Accepted Manuscript

Journal of the Geological Society

Field geology, petrology and geochronology of pluton-dyke systems, the Trapecio and Ushuaia Peninsula dyke swarms (Fuegian Andes): emplacement conditions and relation with tectonics

Mauricio González Guillot, Pablo J. Torres Carbonell, Sebastián Cao, Constanza Lobo, Sofía Bordese & María-Helena B.M. Hollanda

DOI: https://doi.org/10.1144/jgs2023-094

To access the most recent version of this article, please click the DOI URL in the line above. When citing this article please include the above DOI.

Received 27 June 2023
Revised 13 February 2024
Accepted 16 February 2024

Supplementary material at https://doi.org/10.6084/m9.figshare.c.7097733

Field geology, petrology and geochronology of pluton-dyke systems, the Trapecio and Ushuaia Peninsula dyke swarms (Fuegian Andes): emplacement conditions and relation with tectonics

Mauricio GONZÁLEZ GUILLOT[1,2*], Pablo J. TORRES CARBONELL[1], Sebastián CAO[2], Constanza LOBO[1], Sofía BORDESE[3], María-Helena B.M. HOLLANDA[4]

1 Centro Austral de Investigaciones Científicas (CADIC), CONICET, B. Houssay 200 (V9410BFD), Ushuaia, Argentina

2 Instituto de Ciencias Polares, Ambiente y Recursos Naturales, Universidad Nacional de Tierra del Fuego, Antártida e Islas del Atlántico Sur (UNTDF), Fuegia Basket 251 (V9410BFD), Ushuaia, Argentina

3 La.Te.Andes S.A., Vaqueros, Argentina

4 Universidade de São Paulo, IGc, Rua do Lago 562, 05508-080, São Paulo, Brazil

ORCID ID: MGG, 0000-0003-3763-3111; PJTC, 0000-0003-2804-8789; SC, 0000-0003-2307-3993

Present address: S. Bordese, Minera del Carmen S.A., Francisco de Villagra 531 (5400), San Juan, Argentina

*Corresponding author. E-mail: mgonzalez@untdf.edu.ar

Running title: Pluton-dyke systems in the Fuegian Andes

Abstract: We report the field geology, petrography, geochemistry and geochronology data for two dyke swarms in the Fuegian Andes, with the aim of correlating them with known suites and of improving the knowledge on the magmatism of the Late Cretaceous rear-arc and its relation with ductile deformation. We also provide keys for correlation based on amphibole K_2O content. The Trapecio dyke swarm is mildly alkaline and ferriferous, with a zircon U-Pb age of 75 Ma; thus it belongs to the Fuegian Potassic Magmatism (78-68 Ma). The Ushuaia Peninsula dyke swarm, also known as Ushuaia Peninsula Andesites (UPA), was shown to be high-K calc-alkaline and magnesian. New radiometric ages gave 87-86 Ma. While the UPA dyke swarm exhibits foliation associated with ductile deformation, the Trapecio dyke swarm is post-kinematic and reveals emplacement controlled by the slaty cleavage in the metapelite host. Field and geophysical evidence suggest both swarms overlie small upper-crustal plutons, mostly buried. The variable composition of dykes suggests a protracted history of dyke injection, mostly fed from deeper reservoirs. Contact metamorphism around both pluton-dyke systems is very weak. By comparison with adjacent plutons we argue that the main variables controlling aureole development are small magma volumes and low injection rates.

Supplementary material: Full analytical procedures are presented in a pdf file (Online Resource 1). Online Resource 2 provides detailed petrography of the investigated Trapecio dyke swarm samples (Table S1 and Fig. S1), with geochemical data (Table S3 and Fig. S2). Extended petrography and photomicrographs (Fig. S3) of the UPA dyke swarm are provided in Online Resource 3. Mineral chemistry data are reported in Table S2. The results of zircon U-Pb and hornblende Ar-Ar age measurements and ratios are presented in Tables S4 to S8 (Online Resource 4). Thermobarometric results are provided in Table S9.

Dyke swarms are common features above pluton roofs (e.g. Fiske *et al*. 1963; Suárez *et al*. 1987; Giusti *et al*. 2023). The dykes are either fed from within the plutons (e.g. Suárez *et al*. 1987; Jackson and Pollard 1988; Yoshinobu *et al*. 2003) or tapped from deeper reservoirs. In the latter case, the dykes may be either emplaced at the waning stages of pluton construction (Pitcher and Bussell 1985) or during the early stages, thus playing a significant role in building the plutons (e.g. Mahan *et al*. 2003; Glazner *et al*. 2004; Turrillot *et al*. 2011; Bartley *et al*. 2018; Guo *et al*. 2020). Furthermore, the dykes may act as feeder pathways for eruptions (Rhodes *et al*. 2021; Wallrich *et al*. 2023) or may die out upwards (Pitcher and Bussell 1985). In other instances, the dykes may be genetically unrelated with the plutons (Innocenti *et al*. 1997).

Here we study two dyke swarms in the Fuegian Andes that overly small plutons emplaced in the shallow crust, which have scarce exposures or are inferred from aeromagnetic anomalies. These are the Trapecio and the Ushuaia Peninsula dyke swarms, the latter referred to in the literature as the Ushuaia Peninsula Andesites (UPA, González Guillot *et al*. 2011).

Arc magmatism in the Fuegian Andes have received little attention in the geological literature, in part because of the remoteness and inaccessibility of the region. The main units of the Fuegian batholith (Fig. 1a) have been identified and their petrology briefly described in the middle 80's (Hervé *et al*. 1984; Suárez *et al*. 1985, 1987), while most efforts in the last 25 years have been aimed to unveil the timing of pluton emplacement and their relations with the regional tectonic structures (e.g. Cunningham 1995; Klepeis *et al*. 2010; McAtamney *et al*. 2011; Torres Carbonell *et al*. 2020) or to complement palaeomagnetic studies (e.g. Poblete *et al*. 2016; Rapalini *et al*. 2015). The knowledge on the rear-arc magmatism is even more recent, as shown by the fact that most rear-arc plutons have been discovered in the last 15 years (González Guillot *et al*. 2009, 2012). The most recent finding is a Paleocene pluton of the Fuegian batholith on the Navarino island (Velásquez *et al*. 2023).

Petrological knowledge on the Trapecio dyke swarm is limited to preliminary petrographic descriptions (González Guillot *et al*. 2011). This and the UPA dyke swarm crop out 15 km from each other, close to Ushuaia city (Fig. 1), with the Ushuaia pluton in between. The latter belongs to a suite called Fuegian Potassic Magmatism (FPM, González Guillot *et al*. 2009). Both the UPA and FPM are Late Cretaceous rear-arc units (González Guillot 2016), emplaced prior to and after, respectively, a phase of ductile deformation in this region (Torres Carbonell *et al*. 2020).

The mode of emplacement, mineralogical and textural similarities between the Trapecio dykes and the UPA, led González Guillot *et al*. (2011) to correlate them as a single suite. However, the lack of geochemical and geochronological data hindered a precise definition of the Trapecio dyke swarm and its correlation with the known magmatic suites in the area.

In this work, we tackle this problem with new field, petrographical, geochemical and geochronological data of both dyke swarms, including a new age determination for the Ushuaia pluton, with the initial objective of comparing the Trapecio dykes with the Ushuaia pluton and UPA. Our data supports a correlation of the Trapecio dykes with the FPM, based on its U-Pb age of 75 Ma. We also propose the K_2O content of amphibole as a good proxy for correlation between suites across the magmatic arc. We then discuss the possible conditions of emplacement of both Trapecio and UPA dyke swarms by means of geobarometry, simple textural analysis and characteristics of the host-rock. This, along with the new ages provided here, allows us to better constrain the timing of the stage of ductile deformation in the region. We finally discuss the possible link between the dykes and the associated plutons, and the possible factors controlling the development of a small contact aureole by comparison with the large aureole around the Ushuaia pluton (González Guillot *et al*. 2018).

Geological setting

Stratigraphy and tectonic evolution

Jurassic extension and continental break-up in southernmost South America culminated with the opening of a back-arc basin behind a contemporaneous magmatic arc, floored with mid-ocean-ridge-type basalts, named Rocas Verdes (Fig. 1a; Stern and de Wit 2003). The Yahgan Formation is a deep marine succession that represents the clastic infill of the basin during the Early Cretaceous (e.g. Suárez *et al*. 1985; Olivero and Malumián 2008). This unit is exposed along the Beagle channel shore (Fig. 1a), and is the host-rock of the dykes studied in this contribution. At the region of the dyke outcrops, the Yahgan Formation consists of slates from mudstone and sandstone protoliths, with an estimated minimum thickness of 1.5 km (Olivero and Martinioni 1996a).

The closure of the Rocas Verdes basin started around 100-90 Ma, followed by Late Cretaceous arc-continent collision together with lithospheric thickening (Nelson *et al*. 1980; Fildani *et al*. 2003; Klepeis *et al*. 2010), marking the initiation of the Andean orogeny in the region. Basin closure involved a first stage of contractional deformation due to continental underthrusting below the magmatic arc (e.g. Menichetti *et al*. 2008; Klepeis *et al*. 2010; Maloney *et al*. 2011; Torres Carbonell *et al*. 2017). Plutons with ages of 86-83 Ma cross-cut the underthrusting structures in Cordillera Darwin (Fig. 1a) where the deeper structural levels of the orogen are exposed, and at 51-53 °S (Klepeis *et al*. 2010; Calderón *et al*. 2012; Muller *et al*. 2021). However, in the frontal (northern) part of Cordillera Darwin, where shallower levels crop out, cross-cutting relationships and age of syntectonic metamorphic minerals reveal a younger age for this phase of deformation (e.g. Maloney *et al*. 2011). In the study area, the early phase of deformation and metamorphism is recorded by post 87-84 Ma low-grade structures in shallower structural levels (Torres Carbonell *et al*. 2020; this work). Regional metamorphism reached prehnite-pumpellyite facies conditions (e.g. Caminos 1980; Cao *et al*. 2018; Martín *et al*. 2023), whereas to the west, in Cordillera Darwin, it reached amphibolite facies conditions (Nelson *et al*. 1980; Klepeis *et al*. 2010; Maloney *et al*. 2011; Calderón *et al*. 2016).

Recent work postulated that the basement domain of the Fuegian orogenic belt became tectonically consolidated by thrusting postdating the phase of ductile deformation mentioned above (Torres Carbonell and Dimieri 2013; Torres Carbonell *et al*. 2017, 2020). Exhumation associated with thrusting started by *c*. 73 Ma in Cordillera Darwin (e.g. Kohn *et al*. 1995; Klepeis *et al*. 2010; Maloney *et al*. 2011), and propagated shortening towards the foreland fold-thrust belt, terminating in the latest Oligocene to earliest Miocene (e.g. Olivero and Malumián 2008; Barbeau *et al*. 2009; Ghiglione *et al*. 2010; Torres Carbonell *et al*. 2017). The present-day tectonic regime is controlled by left-lateral strike-slip faulting (e.g. Klepeis *et al*. 2010; Torres Carbonell *et al*. 2014).

The Fuegian batholith and the rear-arc in the Fuegian Andes

The Fuegian batholith was constructed episodically from the latest Jurassic to the Paleogene, as a consequence of subduction of the proto-Pacific plate beneath South America (Hervé *et al*. 1984; Suárez *et al*. 1985; Fig. 1a). The calc-alkaline Beagle suite (Hervé *et al*. 1984) is exposed from the cape Horn to northern Navarino island and Cordillera Darwin, showing emplacement ages ranging between 117 and 74 Ma, decreasing with distance from the trench (SERNAGEOMIN 2003). Within this suite, the Castores and Santa Rosa plutons crop out in northern Navarino island, to the south of the study area (Fig. 1a). These are composite intrusions with hornblende gabbros, diorites, quartz diorites-tonalites,

and various generations of basaltic, andesitic and granodioritic dykes (Suárez *et al*. 1987). The plutons gave U-Pb zircon ages of 90-87 Ma (Velásquez *et al*. 2023).

Rear-arc magmatism is represented by two Late Cretaceous suites composed of small intrusions. One is the so called Ushuaia Peninsula Andesites (UPA) that crop out at the Ushuaia peninsula (Fig. 1). It is formed by plugs of hornblendite, diorite, granodiorite and dykes of porphyritic andesite/dacite and hornblende lamprophyre. The suite has a high-K calc-alkaline affinity (González Guillot *et al*. 2011), and ages of 87-84 Ma (González Guillot et al. 2018; this contribution).

The other rear-arc suite is formed by isolated, small, composite plutons, with mildly alkaline, shoshonitic serial character, grouped in the Fuegian Potassic Magmatism (FPM; González Guillot *et al*. 2009). The main intrusive bodies are represented by the Moat, Ushuaia, Jeu-Jepén and Kranck plutons (Fig. 1a), emplaced in a <10 Myr time span, between 78-68 Ma (González Guillot 2016). They all consists mainly of hornblende clinopyroxenite, hornblendite, gabbro/diorite, monzogabbro/monzodiorite and monzonite. There is no evidence of associated volcanic activity with this suite. The Ushuaia pluton (78-71 Ma) was assembled episodically and consists in two main sections. An ultramafic-mafic section includes a large variety of lithotypes, from hornblende clinopyroxenites and hornblendites to gabbro/diorites, plus late stage dykes of monzodiorite-monzonite and lamprophyre compositions. A somewhat younger intermediate section is made of monzodiorite-monzonite rocks and late stage quartz monzonite-granite and lamprophyre dykes (González Guillot *et al*. 2018). This pluton is surrounded by a thermal aureole >2 km wide, with an inner mineral assemblage which includes andalusite, garnet, cordierite, biotite ± sillimanite (fibrolite) and muscovite (González Guillot *et al*. 2018). The pluton contains border facies with peraluminous tonalite and monzogranite with an S-type mineral assemblage, interpreted as hybrids between primary I-type melts and local anatectic melts from the country rock (González Guillot *et al*. 2018; Zuck and González Guillot 2022).

The aeromagnetic map of Tierra del Fuego (chart 5569-II, reduced to the pole; SEGEMAR 1998) shows a small positive magnetic anomaly of 5 x 3 km^2 over the Trapecio lake (with a maximum of 24 nT), elongated in N-S direction (Peroni *et al*. 2016; Fig. 1b). Other FPM plutons define conspicuous positive magnetic anomalies. For instance, an anomaly over 1200 nT is observed in correspondence of the Ushuaia pluton (outcrop area 8.2 km^2, Fig. 1b), and the Kranck pluton area is characterized by a maximum positive anomaly of 75 nT.

Methods

Below we present a brief summary of the various analytical techniques that were employed during this investigation. Detailed information is given in Online Resource 1.

Dyke mapping and lineament analysis

Around 60 % (by number) of the dykes near the Trapecio hill were digitally mapped by analyzing satellite images using Google Earth and Q-Gis softwares (QGIS.org 2021). The remaining dykes and those cropping out at Ushuaia peninsula were mapped and measured on the field. The equal-area projections were constructed with Stereonet software, version 10.4.6 (Allmendinger *et al*. 2013), using field data only.

Petrography and mineral chemistry

A subset of samples of dykes, enclaves and host-rock from both dyke swarms were prepared as standard thin section and observed at the polarizing microscope. Mineral modes were determined by counting 900-1000 points. Grain size nomenclature is after Hibbard (1995), and mineral abbreviations are from Whitney and Evans (2010). The composition of the main mineral phases of the dykes and enclaves was analysed by EPMA (Electron Probe Micro Analyser) at Brasilia University (Brazil, UPA dykes) and at the LAMARX Laboratory of the Córdoba National University (Argentina, Trapecio dykes).

Whole-rock geochemistry

Samples from the Trapecio dyke swarm were selected for whole-rock geochemistry. Major elements were determined by ICP-OES and the trace elements by ICP-MS at Bureau Veritas Mineral Laboratories (Canada) and at Alex Stewart International (Argentina). Geochemical plots were drawn using GCDkit software, version 4.0 (Janousek *et al.* 2006).

Geochronology

Zircon U-Pb ages were obtained by LA-ICP-MS for three samples from the Trapecio and UPA dyke swarms. The data were processed with IsoplotR 5.3 (Vermeesch 2018). Additionally, two Ar-Ar ages on hornblende concentrates were obtained by incremental heating from hornblendites of the UPA and the Ushuaia pluton.

Field features

Trapecio dyke swarm

Several dykes (and to a lesser extent sills) intrude the Yahgan Formation nearby the Trapecio hill. Over 140 tabular bodies were identified on satellite images and on the field, in an area of 5 km^2 (Fig. 2). Fifty-two of them were measured in the field and 41 were sampled. They are 0.1 to 2 m thick (Fig. 3a), but some dykes may reach 4 m in thickness (these contain screens of country rock). Individual lengths vary from few metres to 300 m, although some *en-echelon* segments that could form a single dyke at depth reach altogether up to 1 km. Most correspond to dioritoid dykes (75 %), the remaining correspond to hornblende lamprophyre (<60 cm thick). A small body up to 10 m thick of dioritoid composition shows a lenticular shape and roughly flat bottom (Fig. 3b), which suggests a laccolithic mode of emplacement. Dioritoid and lamprophyre dykes show mutual crosscutting relationships. We hereafter refer to all these bodies as dykes for simplicity.

The dykes are straight traced, show no evidence of ductile tectonic deformation and cut north verging folds and foliation in the Yahgan Formation (Fig. 2b). The contacts are sharp, and many dykes show flow banding parallel to the margins, with oriented crystals and enclaves (Fig. 3c). The general trend is NW-SE (N150°), with high-angle dips (average 73°) to the SW. About 55 % of the dykes show a mean strike of N116° (Figs. 2a and 2c). Dioritoid dykes (n: 40) have a mean dip direction of N226° ± 15°, and 66 % of them dip 72° towards N201° (Fig. 2c-d). The lamprophyres have two distinctive attitudes, one with average strike N111° and dip 72° towards NNE and SSW (n: 6), the other with average strike N4° and dip 81° towards E and W (n: 6) (Fig. 2c-d).

The host-rock shows subtle development of subconchoidal fracture at places, although sedimentary and tectonic features (lamination, axial-plane foliation) are preserved. The general attitude of the tectonic foliation is N107°/66°SW, and is parallel or slightly oblique to the dykes, especially to the dioritoid dykes (Figs. 2d and 3a). The foliation is deflected in the contact with dykes oblique to it, turning parallel to dyke margins due to drag folding.

Ushuaia Peninsula Andesites (UPA dyke swarm)

Holomelanocratic (M' >90 vol. %) to leucocratic (M' >18 vol. %) dykes, plugs and sills are exposed at two abandoned quarries at Ushuaia peninsula (Figs. 1 and 4), and in the proximities, partially covered by vegetation and Quaternary deposits. Discordant forms dominate, thus we also refer to all these intrusions as dykes for simplicity. The main lithotypes are porphyritic andesites and dacites, which form dykes of variable thickness, from few millimetres up to 15 m thick. Other lithologies comprise clinopyroxene hornblendite, hornblendite, gabbro/diorite, melanocratic quartz diorite/monzodiorite, granodiorite and hornblende lamprophyre. They are all holocrystalline. The ultramafic rocks and gabbro/diorite form a 35 m wide plug in the upper bench of the northern quarry, with the former located at the core of the plug (Fig. 4a). The andesite/dacite dykes intrude all other lithotypes, even some lamprophyre dykes (Fig. 4a).

The dykes are subvertical and have variable orientations. However, 72 % of the dykes show preferential orientation, with average strike N22°/76°WNW (Fig. 4c-d). The leucocratic dykes (andesite/dacite) have a mean dip direction between 311°-320° (57 % of the data), whereas the lamprophyre dykes have a mean dip direction between 281°-290° (33 % of the data) (Fig. 4c-d). The dykes are oblique to the country rock foliation (mean attitude N140°/70°SW).

The contacts with the host-rock are generally sharp, straight traced or sinuous (Fig. 5a), occasionally diffuse defining a 3-10 cm mingled margin. The only evidence of contact metamorphism is subtle development of subconchoidal fracture in the metapelite in zones a few tens of centimetres wide around the thickest dykes. Also, no chilled dyke margins were observed (Fig. 5b). The host-rock around the largest intrusive bodies reflects no or very little penetrative deformation (no outcrop-scale folds and occasional spaced rough cleavage). This strongly contrasts with the characteristics of the Yahgan Formation only a few kilometres away from the UPA outcrops, where the rocks are strongly deformed showing several orders of folding, the smallest of which are centimetre-scale folds with closely spaced, axial-planar slaty cleavage (e.g. Torres Carbonell *et al.* 2020). Away from the main outcrops of the UPA, towards the Dos Lomos peninsula (Fig. 1b), the host-rock progressively reveals folding and foliation, which is well developed at the mentioned peninsula, as detailed below.

At Dos Lomos peninsula an andesite dyke crops out, up to 1.5 m thick, with sinuous trace approximately trending NNE-SSW (main trend) and dipping 70° towards N295° (Fig. 4b). The extremities of the dyke accommodate parallel to fractures trending N54°. The most significant feature is that the dyke is surrounded by brecciated material, with irregular distribution but more developed in the footwall side, up to 1 m thick (Figs. 4b and 6a). The breccia is a mixture resulted from *in situ* fragmentation of the host-rock and the dyke. In addition, metasedimentary clasts occur as sparse xenoliths within the dyke (Fig. 6b). Clasts are granule to cobble sized, set in a matrix of sand-sized and finer material. The contact between the dyke and the host-rock is sinuous and cuspate, with indentations of the igneous rock into the metasedimentary rock and vice-versa (Fig. 6b). The igneous clasts in the breccia are flattened (like *fiamme*) and are indented by sedimentary clasts (Fig. 6c) suggesting they were partially molten during breccia formation.

Both the dyke margins and the breccia at Dos Lomos peninsula reveal a tectonic foliation parallel to the host-rock foliation (dip 86° towards 251°). The foliation in the metasedimentary clasts, as well as in the metasedimentary host-rock, is a slaty cleavage, whilst in the dyke margins it is a spaced disjunctive foliation denoted by pressure-solution seams, indicating that deformation occurred after dyke emplacement and breccia formation (see also Torres Carbonell *et al*. 2020).

Petrography

Trapecio dyke swarm

Dioritoid dykes. The dioritoid dykes have porphyritic, seriate to granular textures (Fig. S1a-b). They range from leucocratic to hololeucocratic [colour index (M') 6-32 vol. %], in rare occasions they are mesocratic (M' 38 vol. %). These dykes classify as diorite and monzodiorite, according to the relative abundance of plagioclase and alkali feldspar (Table S1). Porphyritic rocks with fine grained groundmass classify as pheno-andesite. For simplicity, we refer to these compositions as diorite (for diorite and pheno-andesite with Pl phenocrysts) and monzodiorite (for monzodiorite and pheno-andesite with Pl + Afs phenocrysts) hereafter. See Online Resource 2 for additional information.

Plagioclase is the most abundant phase, and in diorites it usually forms the largest crystals (up to 3.5 mm). They are euhedral to subhedral and show multiple zoning. Hornblende is the main mafic phase, although not always present. It forms subhedral to anhedral, green coloured crystals, usually less than 1 mm in length (but may reach up to 3-4 mm), and in some samples they contain scarce biotite inclusions (100-150 μm in length). The monzodiorites contain multiple-zoned, microperthitic alkali feldspar phenocrysts, with abundant inclusions of plagioclase, hornblende and titanite (Fig. S1c).

The groundmass varies in grain size and abundance. In rocks with abundant groundmass (up to 50 vol. %) it is very fine grained (10-20 μm) felsitic (Fig. S1a). In rocks with scarce groundmass it is fine grained (150-400 μm), seriate and interstitial (Fig. S1d). It is composed of plagioclase, variable amounts of alkali feldspar and hornblende, and small amounts of quartz, biotite and accessory phases, such as allanite (in diorites), apatite, titanite, zircon, magnetite and pyrite.

Alteration is moderate to very intense, in the last case with complete obliteration of primary phases and textures. Secondary products are clay minerals, white mica, chlorite, carbonates, epidote, stilpnomelane, anhedral titanite, zoisite/clinozoisite, and secondary amphibole.

Few dioritoid dykes show intense intracrystalline deformation (subgrains, twin dislocations, crystal bending), but sericite flakes have random orientation (both within feldspar crystals and in the groundmass) and thus define no foliation (Fig. S1e). These are dykes with scarce groundmass, where the phenocrysts (oriented or not) are in mutual contact. Dykes in which the phenocrysts do not touch each other lack intracrystalline deformation (Fig. S1a).

Lamprophyre dykes. The lamprophyres are melanocratic dykes (M' ≥65 vol. %), porphyritic, with green hornblende phenocrysts (0.25-3.0 mm in length) with random or preferential orientation (Fig. S1f). Euhedral biotite flakes are included in hornblende. The dykes have intergranular groundmass (20-60 μm) with plagioclase, alkali feldspar, hornblende, magnetite, biotite and apatite. They correspond to the spessartite-vogesite series (Rock 1991).

Enclaves. The dioritoid dykes bear 5-10 cm long mafic microgranular enclaves (MME) and angular to rounded enclaves of medium-grained ultramafic rocks (Fig. 3c-d). The MME are fine-grained (<500 μm), and most of them intensely altered. One MME is a melamonzodiorite composed of green hornblende (>70 vol. %), anhedral plagioclase, perthitic alkali feldspar, biotite, titanite and opaque minerals. The ultramafic enclaves are hornblendite and clinopyroxene hornblendite in composition. The latter contains euhedral to anhedral clinopyroxene crystals surrounded by anhedral hornblende and magnetite (with ilmenite exsolution lamellae). Accessory phases are biotite, titanite and apatite.

Ushuaia Peninsula Andesites

Brief descriptions of the petrography are provided here. See Online Resource 3 and González Guillot et al. (2011) for additional information.

Clinopyroxene hornblendite, hornblendite, gabbro/diorite. These rocks form a single plug with internal transitional contacts. There is a progressive decrease in the content of ferromagnesian minerals, an increase in interstitial material and more poikilitic hornblende towards the outer gabbro/diorite. They are medium- to coarse–grained.

Quartz meladiorite, quartz melamonzodiorite and granodiorite. The melanocratic rocks form small plugs (Fig. 4a) with porphyritic to seriate texture, with hornblende phenocrysts. The granodiorites form thin dykes and breccia infill cross-cutting quartz meladiorite/melamonzodiorite.

Andesite and dacite. They have porphyritic, seriate and microgranular textures (the last two in the thickest intrusions), with plagioclase and hornblende phenocrysts. They contain slate (angular shape), hornblendite and diorite (angular to rounded) centimetre-sized enclaves.

Hornblende lamprophyre. Thin, 10-30 cm thick lamprophyre occur as late-stage dykes (Fig. 4a). They contain oriented hornblende phenocryst and belong to the spessartite-vogesite series (Rock 1991).

Mineral chemistry

Microprobe analyses were carried out for diorite (samples TR10, TR13), monzodiorite (sample TR59) and lamprophyre (sample TR11b) from the Trapecio dyke swarm. Also enclaves of a fine grained melamonzodiorite (MME) and a medium-grained clinopyroxene hornblendite hosted in one diorite dyke (sample TR13) were analysed. From the UPA dyke swarm we analysed an andesite dyke (sample P33) and a magmatic breccia (sample P27-2) with granodiorite infill and quartz melamonzodiorite clasts, cross-cut by a 12 mm-thick dacite dykelet. The results are provided in supplementary Table S2 (see also Table S1).

Trapecio dyke swarm

Calcic amphibole (Fig. 7). The amphibole phenocrysts in the diorite dykes are mainly hastingsite with Mg# [Mg/(Mg+Fe^{2+}) apfu] 0.48-0.31, and magnesiohastingsite with Mg# 0.70-0.52. Microphenocrysts, some phenocrysts rims and groundmass microlites are pargasite and ferropargasite (Mg# 0.60-0.56 and 0.45-0.40, respectively). Secondary actinolite forms rims around some phenocrysts. All magmatic amphiboles have high K content >0.25 apfu (Fig. 7b), with the highest values in hastingsite (*c*. 0.40 apfu). Ti is on average 0.22 apfu.

The amphibole in the melamonzodiorite MME is magnesiohastingsite (Mg# 0.72) with ferropargasite rim (Mg# 0.47). The outermost rim in some crystals is secondary actinolite. In the clinopyroxene hornblendite enclave the amphibole is also magnesiohastingsite (Mg# 0.74) with pargasite rim (Mg# 0.72). The K content is also high in all primary amphiboles (0.21-0.37 apfu), and Ti shows a constant value of 0.23 apfu.

The lamprophyre dykes contain amphibole phenocrysts with multiple zoning. The composition corresponds to magnesiohastingsite and pargasite, with Mg# slightly increasing from core (0.71) to rim (0.73). Potassium content is high (0.34 apfu), and Ti is on average 0.21 apfu. Some phenocrysts have actinolite rims. The amphibole in the groundmass is pargasite (Mg# 0.53).

Feldspars (Fig. 8a). The plagioclase phenocrysts in the diorite dykes show strong multiple zoning. The anorthite content varies from An_{46} to An_{24}. The maximum anorthite content occurs in an inner zone surrounding the core. The cores have compositions in the range An_{36-25}. The outermost rims have the lowest anorthite content. The plagioclase in the groundmass is oligoclase-albite (An_{14-5}).

In the monzodiorite dykes plagioclase phenocrysts show little zonation and the composition is albite (An_{5-7}). Euhedral plagioclase crystals included in alkali feldspar phenocrysts are even more albitic (An_{4-1}). Groundmass plagioclase is similar in composition to phenocrysts (An_{5-8}). Alkali feldspar phenocrysts show uniform composition, with core $Or_{96}Ab_4$ and rim $Or_{97}Ab_3$.

Plagioclase in the melamonzodiorite MME is oligoclase (An_{14}) to pure albite. Perthitic alkali feldspar is $Or_{96}Ab_4$ with exsolution lamellae of albite (An_6). The groundmass in the lamprophyre contains albite (An_5) and orthoclase ($Or_{95-84}Ab_{2-15}$).

Other phases. Biotite (Fig. 8b) is annite-siderophyllite in the diorites [Fe#=Fe^{2+}/(Fe^{2+}+Mg) = 0.46-0.55], lamprophyre (Fe# 0.40) and melamonzodiorite MME (Fe# 0.46), and phlogopite-eastonite in the clinopyroxene hornblendite enclave (Fe# 0.27). Ti is low (<0.25 apfu), especially in the lamprophyre sample (<0.15 apfu).

Clinopyroxene was found only in the ultramafic enclaves. It corresponds to diopside ($Wo_{48}En_{41}$), with Mg# [Mg/(Mg+Fe^{2+})] 0.86. Apatite is fluorapatite, with F 3.4-5.0 wt. % and Cl 0.02 wt. %.

Ushuaia Peninsula Andesites

Calcic amphibole (Fig. 7). Amphibole is mainly magnesiohastingsite in all samples. Andesite amphibole phenocrysts have normal zoning, with Mg# decreasing progressively from core (Mg# 0.86) to rim (Mg# 0.81). K and Ti vary slightly, cores with K 0.23 apfu and Ti 0.18 apfu, rims with K 0.18 apfu, Ti 0.16 apfu. Microphenocrysts have lower Mg# (0.64), but similar K (0.20 apfu) and Ti (0.19 apfu).

The granodiorite hornblende crystals are also normally zoned, with Mg# varying from 0.82 to 0.71 from core to rim. K and Ti are overall homogeneous at 0.18 and 0.16 apfu, respectively. Amphibole in the quartz melamonzodiorite has Mg-richer cores (Mg# 0.87), with darker coloured rims with Mg# 0.78. A profile in a phenocryst (0.8 mm across) shows oscillatory zoning with extremely Mg-rich middle zones (Mg# 0.98). Microphenocrysts and groundmass amphiboles have Mg# 0.88. Ti contents do not vary significantly among zones in phenocrysts or between phenocrysts and groundmass (average Ti is 0.16 apfu). Conversely, K contents vary slightly between 0.20 apfu and 0.17 apfu (Fig. 7b).

Amphibole phenocrysts in the dacite dykelet are normally zoned, although some crystals show oscillatory zoning. The cores are magnesiohastingsite, while rims and inner zones close to rims are magnesiohastingsite, magnesiohornblende or tschermakite. Phenocryst cores have Mg# 0.85 and rims have Mg# 0.71, middle parts have intermediate compositions. Microphenocryst cores have Mg# 0.61. Potassium content is slightly higher in phenocryst and microphenocryst cores (0.20 apfu) than in rims (0.18 apfu in magnesiohastingsite). Ti is in the range of 0.16-0.21 apfu.

Feldspars (Fig. 8a). Plagioclase phenocrysts in the andesite dyke are andesine-oligoclase. They show oscillatory zoning, with cores An_{30-22} (except for one single datum with An_{17}) and more calcic rims (An_{36-28}). One crystal has rims of An_{49-46}. Middle zones in phenocrysts are An_{32-22}. Microphenocrysts have cores of An_{44-34}.

Plagioclase in the dacite dykelet is oligoclase-albite. Phenocrysts and microphenocrysts have cores of An_{10}, and rims of $An_{4-6}Ab_{95-93}$. In the granodiorite it is oligoclase, with normal zoning, less significant than in andesite. Phenocrysts have core – rim compositions of An_{21-15} and An_{13}, respectively. Interstitial plagioclase is An_{15}. Plagioclase microphenocrysts in the quartz melamonzodiorite have oligoclase rims (An_{19}). The cores are usually altered but a single, fresh grain yielded An_{76}.

Alkali feldspar is orthoclase in all samples. In the dacite dykelet it has core compositions of $Or_{95-81}Ab_{3-18}$ and rim compositions of $Or_{87-83}Ab_{12-17}$. In the granodiorite it is $Or_{97-85}Ab_{3-14}$. Alkali feldspar in the quartz melamonzodiorite is $Or_{99-62}Ab_{1-38}$.

Other phases. Biotite was analysed in the andesite dyke only, it is annite-siderophyllite (Fig. 8b), with Fe# 0.45. Al^{iv} (2.64 apfu), Ti (0.44-0.47 apfu, rim and core respectively) and Cl (0.05 wt. %) contents are higher with respect to biotite crystals from the Trapecio dyke samples, whereas Si (5.36 apfu), K (1.76 apfu) and F (0.08 wt. %) are lower.

Two clinopyroxene grains were analysed in the quartz melamonzodiorite, found as inclusions in hornblende. The composition corresponds to diopside ($Wo_{46}En_{45}$), with Mg# (0.95), slightly higher than the analysed clinopyroxene crystals from the Trapecio clinopyroxene hornblendite enclave. Apatite was analysed in the andesite and dacite. It is fluorapatite with lower F (2.1-3.8 wt. %) and higher Cl (0.16 wt. %) than in the Trapecio dykes.

Allanite is a ubiquitous accessory phase in the UPA dyke swarm samples as microphenocrysts or in the groundmass. Allanite crystals have rather constant total REE (ΣREE) around 14.51 wt. % in the andesite-dacite dykes, and more variable in the granodiorite, from 17.12 to 9.21 wt. %. The most abundant REE is Ce (Ce_2O_3 4.98-8.80 wt. %).

Whole-rock geochemistry (Trapecio dyke swarm)

Six samples were analysed for the Trapecio dyke swarm, three diorites, two monzodiorites and one lamprophyre (Table S3). Whole-rock geochemistry for the UPA dyke swarm is reported in González Guillot et al. (2011), and comparisons between both dyke swarms is given below in the Discussion.

The SiO_2 content varies from 49 wt. % (lamprophyre) to 60 wt. % (diorites and monzodiorites). The LOI is moderate to high (1.6-4.4 wt. %), in agreement with the intense alteration observed in most dykes. The TAS (total alkali-silica) classification indicates these rocks are monzonites and quartz monzonites, while the lamprophyre corresponds to gabbro (Fig. 9a). However, for the sake of simplicity we prefer to maintain the modal nomenclature identified by petrography (Table S1).

The samples define a mildly alkaline magma series in the TAS diagram (Fig. 9a), with K_2O contents corresponding to high-K calc-alkaline series (Fig. 9b) (somewhat lower than expected, see Discussion). The K_2O/Na_2O ratio varies from 0.47 to 0.80 (Table S3). They are metaluminous and ferriferous (Fig. S2a-b). The Mg# is rather constant and low, in the range 0.32-0.37 (molar), with MgO 1.56-0.83 wt. % (Table S3). The lamprophyre, as expected, is significantly richer in MgO (Mg# 0.52, MgO 5.98 wt. %).

While alkalis show a positive correlation with SiO_2, the other major oxides decrease as SiO_2 increases, with rather continuous linear trends (Fig. 9). Al_2O_3 increases from the lamprophyre to the diorite samples, but does not define a clear trend among the diorite-monzodiorite samples (Fig. 9c). The CaO/Al_2O_3 ratio also decreases with increasing SiO_2 (Fig. 10a).

Compatible trace elements, such as V, Co and Sc show negative correlation with SiO_2, whereas the ratio V/Co increases with SiO_2 (Fig 10b-e). Incompatible trace element ratios, such as Th/La and Ti/P (Fig. 10f-g), remain roughly constant with increasing SiO_2, while other ratios, such as Zr/Nb and to a lesser extent Zr/Hf (Fig. 10h-i) increase with increasing SiO_2.

Trace elements normalized to primitive mantle (Sun and McDonough 1989; Fig. 11a) show enrichment in LILE (large ion lithophile elements) relative to HFSE (high field strength elements), and conspicuous negative peaks at Nb-Ta [$Nb^* = Nb_N/(K_N \cdot La_N)^{0.5}$= 0.37-0.04] and Ti, and a positive peak at Sr. Dioritoid samples define homogeneous patterns, whereas the lamprophyre dyke shows lesser enrichment in LILE (from Rb to K) and slightly higher Ti and Dy values.

The REE (rare earth elements) normalized to chondrite (Sun and McDonough 1989) show enrichment of LREE (light) with respect to HREE (heavy), with $(La/Yb)_N$ 5.09-14.79 (Table S3; Fig. 11b). The samples are slightly to moderately enriched in LREE relative to the MREE (medium) [$(La/Sm)_N$ 1.65-4.77], whereas they show an overall flat pattern in the MREE-HREE region, with MREE/HREE ratios from slightly enriched to slightly depleted [$(Dy/Yb)_N$ 0.90-1.45]. The lamprophyre dyke is less LREE and more MREE enriched than dioritoid dykes, whereas the monzodiorites are more MREE depleted than the other samples. The Eu anomaly in all samples is small to negligible [$Eu^* = Eu_N/(Sm_N \cdot Gd_N)^{0.5}$ = 0.89-1.03].

Geochronology

Below we provide U-Pb zircon ages for the Trapecio and the UPA dyke swarms, and two Ar-Ar hornblende ages for the UPA and the Ushuaia pluton (location of samples in Figs. 1b-2 and 4). The full analytical results are provided as supplementary files (Tables S4-S8, Online Resource 4). A previous U-Pb zircon age from an andesite/dacite UPA dyke (sample P16) yielded 84.1 ± 1.6 Ma (González Guillot *et al*. 2018).

Sample TR59 (monzodiorite, Trapecio dyke swarm)

The separated zircon crystals are 150-200 μm across, euhedral, generally clear (colourless to yellow), prismatic grains with subrounded edges, with no visible inherited cores. They show fractures and inclusions. On a total of 99 analysed points, 66 spots show concordance within 100 ± 10 % between $^{206}Pb/^{238}U$ and $^{207}Pb/^{235}U$ data. The 206/238 ages span from 67 to 284 Ma, 60 of which span from 71 to 89 Ma. Three grains span from 140 to 156 Ma and a single grain yields 284 Ma, which may reflect contamination by Yahgan and/or Lemaire formations. Two grains around 67-68 Ma probably reflect Pb loss. After filtering, a population of 38 spots, ranging from 71 Ma to 79 Ma, gave a weighted mean $^{206}Pb/^{238}U$ age of 74.56 ± 0.35 Ma (2σ), mean squared weighted deviation (MSDW) 7 (Fig. 12a-b), which we interpret as the age of emplacement and crystallization of the dyke. The large dispersion of the data, especially the ages around 84-89 Ma, may be caused by incorporation of microenclaves or disaggregated xenocrysts/antecrysts, which are difficult to separate during sample preparation.

Sample 261 (andesite dyke, UPA)

This sample belongs to the dyke that forms the hybrid breccia at Dos Lomos peninsula. The sample was taken from the core of the dyke, excluding margins and breccia fragments. The separated zircon crystals are 100-200 μm across, euhedral to subhedral; most of them appear clear, pinkish, prismatic grains with subrounded edges, fractures and no visible inherited cores. Thirty-one spots out of forty-nine show concordance within 100 ± 10 % between $^{206}Pb/^{238}U$ and $^{207}Pb/^{235}U$ data. The 206/238 ages span from 84 to 283 Ma, 30 of which span from 84 to 96 Ma. Four grains with 94-96 Ma and one with 283 Ma may reflect country rock assimilation as in the previous case. After filtering, a population in the range 86-92 Ma (15 spots), gave a $^{206}Pb/^{238}U$ age of 88.17 ± 0.55 Ma (2σ), MSDW 3.5. A subset of 11 grains in the range 86-89 Ma gave a 206/238 weighted mean age of 87.46 ± 0.55 Ma (2σ), MSDW 1.8 (Fig. 12c-d), which we interpret as the age of emplacement and crystallization of the dyke.

Sample P30 (andesite/dacite dyke, UPA)

The analysed zircon crystals are 50-200 μm across, complete euhedral to subhedral, or broken during crushing; most of them clear, stubby square prismatic grains with simple terminations, and no visible inherited cores. They commonly show growth zoning. The concordant (±10 %) spots range from 81 to 152 Ma. A population with $^{206}Pb/^{238}U$ ages around 108-115 Ma, and a single grain of 152 Ma are interpreted as possible inheritance from Yahgan and Lemaire formations, respectively. One grain with 81 Ma may reflect Pb loss. After filtering, 20 points with $^{206}Pb/^{238}U$ ages between 85 and 91 Ma gave a weighted mean age of 87.30 ± 0.54 Ma (2σ) (MSWD 2.3). A subset of 14 grains in the range 85-88 Ma gave a 206/238 weighted mean age of 86.34 ± 0.64 Ma (2σ), MSDW 0.69 (Fig. 12e-f), indistinguishable from the previous sample. We interpret the last result as the age of emplacement and crystallization of the dyke.

Sample MP6 (hornblendite, UPA)

This sample comes from a coarse-grained hornblendite plug (Fig. 4a). The weighted mean age is 86.73 ± 1.5 Ma (2σ), MSWD 3.79 (Fig. 12g). A duplicate yielded 87.86 ± 1.33 Ma. These data represent the cooling age, which is indistinguishable from the U-Pb zircon ages of the andesite/dacite dykes.

Sample MTC298B (Cpx hornblendite, Ushuaia pluton)

This sample belongs to a coarse-grained clinopyroxene hornblendite from the Ushuaia pluton (ultramafic-mafic section), which contains pegmatitic hornblendite pockets with diffuse and sinuous contacts. The weighted mean age is 77.52 ±1.27 Ma (2σ), MSWD 14.4 (Fig. 12h). A duplicate yielded 77.93 ± 1.29 Ma, MSWD 11.66. We consider these results as the cooling age of the rock.

This age is similar or slightly older than that obtained for a pegmatitic gabbro pocket segregated in a hornblende pyroxenite located 170 m to the NE from sample MTC298B, which yielded a U-Pb zircon age of 75 ±1 Ma (González Guillot *et al*. 2018). Other reported ages for the Ushuaia pluton range from 74.7 + 2.2 / - 2.0 Ma to 70.9 ± 1.7 Ma (U-Pb in zircon, Barbeau *et al*. 2009; González Guillot *et al*. 2018).

In summary, our geochronological results reveal that the emplacement of the Trapecio dykes is overall contemporaneous with that of the Ushuaia pluton. Additionally, the results indicate that the hornblendite plug from the Ushuaia peninsula quarry likely belongs to the UPA suite. The plug was previously ascribed to Ushuaia pluton by González Guillot et al. (2011), based on cross-cutting relationships and whole-rock K-Ar ages (see discussion on K-Ar ages in González Guillot *et al*. 2018).

Discussion

Correlation of the Trapecio dyke swarm with other magmatic suites of the Fuegian Andes (UPA and FPM)

The UPA dyke swarm represents a unique suite in the rear-arc of the Fuegian Andes (González Guillot *et al*. 2011). The reported ages indicate it was emplaced at least 3.7 Myr earlier than the Ushuaia pluton, and thus it predates the FPM. It is contemporaneous with the last pulses of the Santa Rosa and Castores plutons (90-87 Ma) of the Beagle suite (Suárez *et al*. 1987; Velásquez *et al*. 2023), and a correlation between them was recently established (Velásquez *et al*. 2023).

The Trapecio dyke swarm was previously correlated with the UPA, based on mode of emplacement, petrography and proximity (González Guillot *et al*. 2011). However, the geochemical characteristics and the ages reported here reject that correlation and instead suggest the Trapecio dyke swarm belongs to the FPM. Both are mildly alkaline (Fig. 6a) and ferriferous (Fig. S2b), whereas the UPA is subalkaline (Fig. 6a) and magnesian (Fig. S2b).

The Trapecio dyke swarm is less K_2O-rich than the FPM plutons, which could be due to mobility of K during alteration (in agreement with the high LOI). However, the K_2O (for similar SiO_2 contents) is higher than in the UPA dyke swarm (Fig. 9b). Compatible trace elements (Cr, Ni, Co) are lower (for similar SiO_2) in the Trapecio dyke swarm and in the Ushuaia pluton than in the UPA (e.g. Fig. 10c). The Trapecio dyke swarm samples also show different slopes in the V/Co and Zr/Nb ratios against SiO_2 than the UPA samples (Fig. 10e, 10h).

Mineral chemistry also demonstrates that the Trapecio dyke swarm belongs to the FPM. Potassium content in amphibole has been used to discriminate parental magma compositions, in which the more K rich the amphibole, the more K rich the magma from which it crystallized (González Guillot *et al*. 2012; González Guillot 2016). Figure 7b shows that magnesiohastingsite, pargasite and ferropargasite crystals of the Trapecio dyke swarm and FPM plutons have similar K content, and are noticeably higher

than in the UPA dyke swarm and in calc-alkaline plutons of the Fuegian batholith (Torres García *et al*. 2020). Amphiboles from the Trapecio dyke swarm and FPM plutons have also higher K/Na ratios (average 0.54) than amphiboles from the UPA dyke swarm (average 0.29). This is consistent with amphiboles crystallizing from mildly alkaline and calc-alkaline magmas, respectively (Molina *et al*. 2009; Bonechi *et al*. 2017; see also Ridolfi and Renzulli 2012).

Interestingly, Molina *et al*. (2009) argued that TiO_2 content of calcic amphiboles is the most useful discriminant between alkaline and calc-alkaline parental magmas, even better than the K_2O content (for a given TiO_2 composition). They include in the alkaline branch mildly alkaline compositions and what they call 'subalkaline trachytoids', a rock series falling immediately below the line dividing the alkaline and subalkaline field in a TAS diagram, similar to the UPA. The TiO_2 content of amphiboles from the Trapecio dyke swarm, the FPM plutons and the UPA show large overlap. Therefore, our data demonstrate that potassium is instead more efficient than titanium in discriminating between amphibole crystals crystallizing from mildly alkaline, high-K calc-alkaline or normal calc-alkaline magmas. Figure 7b presents lines dividing the fields for amphiboles crystallized from such magmas, based on compositions from the Trapecio and UPA dyke swarms (this work), FPM plutons (authors' unpublished data) and the Fuegian batholith (Torres García *et al*. 2020).

A question now arises: is the Trapecio dyke swarm part of the Ushuaia pluton, i.e. the roof system of the intrusion? An affirmative answer may be suggested by analogy with the Kranck pluton (FPM, González Guillot *et al*. 2012; Fig. 1a), which is surrounded to the north by a dyke swarm that extends up to 6 km from the pluton margins, with increasing dyke density towards the pluton. It has been interpreted as a pluton-dyke system based on similar ages and compositions (Torres Carbonell *et al*. 2020). The Trapecio dyke swarm is also 6 km from the Ushuaia pluton. However, it is located to the ENE (Fig. 1). This position cannot be attributed to displacement associated with the NNE vergence of the Andean tectonics (e.g. Cao *et al*. 2023) or the sinistral Cenozoic strike-slip faulting that took place after the Andean contraction (Menichetti *et al*. 2008; Torres Carbonell *et al*. 2014). Besides, no dykes were identified between the Trapecio hill and the Ushuaia pluton (except for a single hornblende lamprophyre halfway between them; authors' unpublished data), and there is no connection between the aeromagnetic anomalies over both magmatic units (Fig. 1b).

Actually, geochemical differences between the Trapecio dyke swarm and both sections of the Ushuaia pluton do indeed exist. For instance, rock samples from the Trapecio dyke swarm and the intermediate section of the Ushuaia pluton have slightly higher MnO, CaO/Al_2O_3 and lower Ti/P content and ratios for a given SiO_2 value compared with the ultramafic-mafic section (Figs. 9h, 10a, 10g). However, the Trapecio dyke swarm samples show a rather constant increase in Sr and V/Co (Fig. 10e) with increasing SiO_2, similar to the ultramafic-mafic section of the Ushuaia pluton, whereas the intermediate section shows a somewhat constant V/Co ratio (Fig. 10e). Increasing V/Co suggests clinopyroxene fractionation (also decreasing CaO/Al_2O_3), whereas a decrease (such as in the UPA) would indicate amphibole fractionation. This is supported by mineral-melt partition coefficients, which are 1.1-5.2 and 6.3-13.0 for V and 5.55 and 1.77-6.1 for Co, for Cpx-andesite and Amp-andesite, respectively (GERM Database). Additionally, the Trapecio dyke swarm samples have lower MREE in normalized diagrams than those from both sections of the Ushuaia pluton (Fig. 11b). Also, late-stage monzodiorite segregations of the ultramafic-mafic section of the Ushuaia pluton have REE patterns different to Trapecio dyke swarm samples (Fig. 11b).

The above evidence suggests that the Trapecio dyke swarm belongs to an independent unit within the FPM. Thus, the dykes are not part of the roof system of the Ushuaia pluton, but likely the roof system of another, similar pluton that resides at subsurface levels, the Trapecio pluton. The presence of this body is hinted by the mafic-ultramafic angular enclaves hosted in the dykes (Fig. 3d) and by the

aeromagnetic anomaly (Peroni *et al.* 2016), which suggests the pluton lies at a shallow depth and has limited vertical extension.

The elevation difference between the Ushuaia pluton (its highest exposure is 380 m a.s.l.) and the Trapecio dyke swarm (the lowest dykes are on average at 700 m a.s.l.) is 320 m. The Ushuaia pluton is believed to be eroded at or very close to the roof level (González Guillot *et al.* 2018). It was eroded by the northern side of the >1000 m thick Beagle discharge palaeoglacier (Rabassa *et al.* 2000; Isla *et al.* 2001), while the Trapecio hill was affected only by a local cirque glacier, which originated on its summit (A. Coronato pers. com.). This explains the lower erosion level at Trapecio hill and why the Trapecio pluton does not crop out. It is then possible that the roof of the Trapecio pluton is only 320 m below the floor of the cirque (Fig. 13). In that case, the metamorphic aureole should be of limited extension (as in the Kranck pluton; González Guillot *et al.* 2012). Inferences on the contact aureole are resumed below.

Emplacement conditions of Trapecio and UPA dyke swarms and their relation with regional tectonics

The UPA dyke swarm was emplaced prior to the main stage of ductile deformation in this part of the Fuegian Andes (Torres Carbonell *et al.* 2020; this work). The fact that the dykes are oblique to the slaty cleavage (Fig. 4c-d) holds this statement. On the contrary, the majority of the Trapecio dykes are subparallel or parallel to the slaty cleavage (Fig. 2), which suggests that magma emplacement was controlled preferentially by the prior planes of weakness formed by the tectonic foliation in the country rock.

Therefore, the Trapecio dyke swarm emplaced after this phase of deformation and peak regional metamorphism, which is of very low grade in the study area (Caminos 1980; Cao *et al.* 2018; Torres Carbonell *et al.* 2020; Martín *et al.* 2023). Despite this, dykes with high phenocryst content show ductile deformation (Fig. S1e), and most contain primary mineral phases that appear to be retrogressed to low-T greenschist facies conditions (Ab-rich plagioclase, chlorite, epidote and actinolite after hornblende and biotite). However, we interpret the ductile deformation not as due to regional tectonics, but as a submagmatic fabric, developed during emplacement of a crystal cargo and further compaction during interstitial melt extraction (cf. Fiedrich et al. 2017). This process led to interference and plastic deformation of phenocrysts without significant development of foliation. Similarly, we interpret the alteration to be deuteric, as is usual in fluid-rich intrusions (Rock 1991). Some dykes may have efficiently lost their volatiles before complete crystallization while others did not, resulting in large variation in degrees of alteration among dykes. The prehnite-pumpellyite facies conditions in the host-rock and the random orientation of sericite flakes in the dykes (both in groundmass and within phenocrysts; Fig. S1e) rule out a metamorphic origin of the secondary minerals.

The timing of ductile deformation and peak regional metamorphism associated to underthrusting during the closure of the Rocas Verdes basin has complex interpretations away from our study area. While ductile structures have been reported to predate 83-86 Ma Beagle suite intrusives in some parts of Cordillera Darwin and further north (53-52 °S; Klepeis *et al.* 2010; Calderón *et al.* 2012; Muller *et al.* 2021), peak metamorphism (>600 °C) as young as 73 Ma was also reported in Cordillera Darwin (Maloney *et al.* 2011). A diachronic progressive deformation from deeper to shallower levels in the orogen is not ruled out; accordingly, our data reveal that ductile deformation acted in the study area (i.e. shallower and forelandward structural horizons compared to Cordillera Darwin) between 87-84

Ma (UPA) and 78-71 Ma (the age range of the Ushuaia pluton and Trapecio dyke swarm). These ages are consistent with previous age constraints and interpretations on the mode of deformation of the Fuegian Andes during the closure of the Rocas Verdes basin (Torres Carbonell *et al.* 2020).

In order to obtain the conditions of crystallization, the emplacement levels and the approximate temperature contrast with the host-rock, temperature and pressure were estimated for the Trapecio and UPA dyke swarms (Table S9). We used formulations based on a single phase composition, since those calibrated on the equilibrium of two or more phases can be hardly applicable to hybrid and variously re-homogenized magmas (Ridolfi *et al*. 2010; Gorini *et al*. 2018), which is the case we infer for both dyke swarms. The amphibole geothermometers (Ridolfi and Renzulli 2012; Putirka 2016, eq. 5; Ridolfi 2021) and geobarometers (Ridolfi *et al*. 2010; Ridolfi and Renzulli 2012; Krawczynski *et al*. 2012) employed yield the conditions of crystal saturation, so we used the most Mg rich amphiboles [Mg# (Mg/(Mg+Fet) apfu) >0.5]. Erdman *et al*. (2014) and Molina *et al*. (2021) indicated these thermometers give realistic results. However, the amphibole-only multi-component barometers from Ridolfi *et al*. (2010) and Ridolfi and Renzulli (2012) have been criticized (Erdman *et al*. 2014; Molina *et al*. 2021), although Gorini *et al*. (2018) proposed a method to improve the results (see Online Resource 1).

Average temperature estimates vary from 934 °C to 972 °C for the lamprophyre and diorite samples from the Trapecio dyke swarm. After selecting homogeneous compositional zones within amphibole crystals (cf. Gorini *et al*. 2018), the average temperature for the lamprophyre is 940 °C (no homogeneous zones in crystals from the diorite were found). The mafic and ultramafic enclaves in the diorite yielded average temperatures from 931 °C to 973 °C (average 925 °C within homogeneous zones in crystals from the ultramafic enclave). Clinopyroxene in the ultramafic enclave yielded 1154 °C [eq. 32d (Putirka 2008) at 7 kbar, see below].

Samples from the UPA dyke swarm yielded slightly higher temperature estimates, on average 30 °C (which is almost within the calibration errors, ±30-22 °C). The andesite and dacite dykes yielded a range of 932-985 °C average temperatures. By selecting homogeneous zones in crystals of the andesite, an average temperature of 957 °C is obtained. The granodiorite gave average temperatures of 947-969 °C, but homogeneous zones in hornblende crystals yielded an average temperature of 934 °C. The quartz monzodiorite yielded an average temperature of 1010 °C for homogeneous zones in hornblende crystals.

Pressures for the lamprophyre and the ultramafic enclave from the Trapecio dyke swarm gave similar results around 4 kbar (3.7 kbar and 4.0 kbar, respectively, with Krawczynski *et a*l. (2012) formulation). The diorite (which hosts the enclave) yielded a much higher pressure value (7.0 kbar). The Ridolfi (2021) Hbl-only barometer applied to homogeneous zones with Mg# >0.62 within hornblende crystals, yielded average pressures of 7.7 kbar and 7.2 kbar (eq. 1d) for the lamprophyre and the ultramafic enclave.

Barometry results obtained using the Krawczynski *et al*. (2012) formulation for the UPA dyke swarm (Hbl Mg# >0.6) range from 4.6 kbar to 6.4 kbar. The geobarometer of Ridolfi (2021, eqs. 1d and 1e, with the procedure described in Gorini *et al*. 2018) gave pressures from 6.5 kbar to 13.0 kbar.

It should be taken into account that equations 1d and 1e of Ridolfi and Renzulli (2012) tend to overestimate pressure (Erdman *et al*. 2014; Molina *et al*. 2021). An empirical barometer based on total Al in biotite (Uchida *et al*. 2007), gave solidification pressures of 2.0-1.4 kbar and 1.8 kbar (±0.33) for the Trapecio and UPA dyke swarms, respectively.

The pressure estimates for the Trapecio and UPA dyke swarms show that hornblende phenocrysts (or antecrysts) nucleated at *c.* 7 kbar, or 27 km depth (assuming an average density of the local crust of 2700 kg m^{-3}), i.e. in the mid-lower crust in both suites. Alkalis content greater than 2.5 wt. % in the amphiboles of the Trapecio and UPA dyke swarms and the Ushuaia pluton (Table S2, Fig. 9a) is consistent with high pressure of crystallization (Ridolfi *et al.* 2010). However, pressure of emplacement is supposed to be much lower, in the upper crust. The Ushuaia pluton is assumed to be emplaced between 2.5 and 3.5 kbar, based on the same hornblende barometers employed here and on the contact aureole paragenesis (González Guillot *et al.* 2018; Torres García *et al.* 2020), most probably closer to 2.5 kbar (González Guillot *et al.* 2018). We assume a similar emplacement level for the Trapecio dyke swarm, supported by their similar country rock and age, and their proximity. This means that the dykes emplaced as a crystal cargo at *c.* 9.5 km, and further crystallization occurred *in situ*. However, the emplacement level of the UPA dyke swarm deserves additional discussion.

The breccia around the dyke at Dos Lomos peninsula (Figs. 4b and 6) is a key element to consider. The presence of both sedimentary and igneous clasts is typical of heterobreccias (Delaney and Pollard 1981). Additionally, the presence of angular clasts of only local Yahgan Formation suggests little transport. We also observed that the igneous clasts are lenticular, deformed fragments, and that the dyke also contains irregular xenoliths of the host-rock (Fig. 6). Altogether, the data suggest that the breccia formed *in situ* during dyke intrusion. It may be interpreted as a peperite, thus pointing to a very shallow emplacement, since peperite forms as magma intrudes unconsolidated (or poorly consolidated), water-saturated sediments at or close to the sediment-water interface (White *et al.* 2000). However, the absence of (i) *in situ* fragmentation of the dyke along its margins (jigsaw-fit texture), (ii) injections of fluidized sediment into the dyke, and (iii) a selvedge of glass around igneous clasts or dyke margins is at odds with this. Besides, the minimum age estimated for the sedimentation of the Yahgan Formation in this area is at least 12 Myr older than the UPA. It is around 105 Ma, based on detrital zircon age populations (Barbeau *et al.* 2009 and our unpublished data) and on late Albian (*c.* 105-100 Ma) inoceramids occurring east of the study area (Olivero and Martinioni 1996b).

An alternative process is brecciation by fragmentation and fluidization of consolidated rock due to sudden and explosive degassing. This is common in volatile rich magmas, like the appinite associations (H_2O dominated fluid; Platten 1984; Rock 1991; Pitcher 1993), and kimberlite intrusions (CO_2 dominated fluid; Wilson and Head 2003; Sparks *et al.* 2006; Barnett *et al.* 2011). Brecciation may also be triggered by boiling of pore fluid (meteoric water) in the host-rocks by thermal perturbations due to arrival of magma (e.g. Hoyer and Watkins 2016). The genesis of maar-diatreme volcanoes (Lorenz and Kurszlaukis 2007; Valentine *et al.* 2014) or hydrothermal vent complexes associated with sill emplacement in sedimentary basins (Jamtveit *et al.* 2004; Schofield *et al.* 2012) provide further examples of the process. Most authors postulate very shallow conditions for the expansion of the gas phase to be able to overcome the mechanical strength of the country rock and to produce brecciation, to a threshold depth limit of 2.2 km (Delaney and Pollard 1981; Jamtveit *et al.* 2004; Schofield *et al.* 2012). Platten (1984) concluded that brecciation due to boiling of juvenile water at high temperature along appinite intrusions occurred at similar shallow depths, possibly at 1.0 or 0.5 kbar (3.8-1.9 km). However, if the fluid phase is rich in CO_2, brecciation may occur substantially deeper due to the lower solubility of CO_2 in silicate melts compared to H_2O (Wilson and Head 2003, 2007).

The absence of vesicles and chilled margins in the dykes (Fig. 5b), and the fact that the host-rock was already consolidated, rule out a shallow level for dyke emplacement and breccia formation. Moreover, hornblende is not stable at very low pressure, and the presence of hornblende in the ultramafic plug and in the coarse-grained seriate groundmass (>100 μm) of andesites (Fig. S3d), inferred to have crystallized *in situ*, indicate pressures greater than 1 kbar (3.8 km), for water-

saturated, andesitic-dacitic magmas at 950 °C (e.g. Cashman and Blundy 2000). Therefore, we propose that brecciation and dyke emplacement occurred at a somewhat higher pressure than proposed in the literature, possibly at 1.8 kbar (6.8 km), based on biotite barometry.

Exsolution of juvenile fluids and outgassing occurs mainly when the magma reaches intermediate to high crystal fractions (Parmigiani *et al*. 2017). We assume that fluid exsolution and outgassing in UPA occurred after dyke emplacement and before complete crystallization due to volatile saturation (second boiling), in the case of the andesite-dacite dykes. Indeed, we suggested that the system was at a depth of 6.8 km, so too deep to respond to removal of load by gravitational processes at the sea floor. Further, the region was experiencing tectonic burying at the time of emplacement (e.g. Klepeis *et al*. 2010; Maloney *et al*. 2011; Torres Carbonell *et al*. 2020). Additionally, very fine, aphanitic groundmass is recognized only in some andesite/dacite dykes (Fig. S3c), whereas other dykes are seriate to granular, medium- to coarse-grained (Fig. S3a, b, d).

Upon outgassing, rapid crystallization occurred, leading to the formation of the aphanitic groundmasses (cf. Cashman and Blundy 2000). Exsolution after much of the crystallization stage also explains the elevated porphyricity (30-45 % phenocryst) of the andesite/dacite dykes, even in millimetre-thick dykelets with phenocryst as large as the width of the dyke (Figs. 5b and S3c).

Construction of the pluton-dyke systems

What do the Trapecio and UPA dyke swarms represent in relation with the associated plutons? Dykes emplaced at pluton roofs in the shallow crust have different origins. Some are fed from within the plutons (e.g. Rhodes *et al*. 2021; Wallrich *et al*. 2023), others are fed from deeper, co-magmatic reservoirs in the mid-lower crust, either at the waning stages or after pluton crystallization (Pitcher and Wallace 1985), or from the early stages of pluton construction (Glazner *et al*. 2004; Guo *et al*. 2020).

We interpret that the outcrops at Ushuaia peninsula represent the cupola of a small pluton, most of which is buried (Fig. 13). The ultramafic-mafic plug in the upper bench of the quarry (Fig. 4a) represents an apophysis of the pluton, and the transitional gradation from pyroxene hornblendite to gabbro/diorite suggests small-scale *in situ* differentiation. The cupola was successively cut by crystal-laden batches of magma that crystallized as porphyritic quartz diorite-monzodiorite, granodiorite and finally andesite/dacite-lamprophyre. The hornblende barometry suggests they were delivered from mid-lower crustal reservoirs, which were subjected to repeated replenishments, as evidenced by the oscillatory zoning in plagioclase and hornblende phenocrysts. Emplacement of magmas with an elevated crystal cargo formed in deeper reservoirs is a common process (e.g. Leuthold *et al.* 2014). Additionally, the sharp contacts among these intrusions suggest that previous injections were already crystallized at the moment the new ones arrived. The pluton is not evidenced by an aeromagnetic anomaly (Fig. 1b), which may be due to the fact that the opaque phases are dominated by sulphides (Online Resource 3), contrarily to the FPM plutons, which contain magnetite (González Guillot *et al.* 2018).

Similarly, we envisage the Trapecio dykes were derived from mid/lower-crustal reservoirs and cross-cut the pluton in the shallow crust (Fig. 13), from which they incorporated most of the enclaves. The mingling observed in some dykes (Fig. 3c) suggests the same conduits were used by magma batches of different composition (e.g. Alasino *et al*. 2017; Glazner and McNutt 2021). Other dykes with evolved monzodiorite composition may indicate tapping from a transient magma reservoir within the pluton, subject to small-scale differentiation.

The broad variety of dyke compositions embraces large part of the lithologies of contemporaneous and related intrusions (Trapecio dykes and Ushuaia pluton, UPA dykes and Santa Rosa and Castores plutons). This suggests a protracted history of dyke injection during assembly of the Trapecio and UPA pluton-dyke systems. A similar situation occurs with the Kranck pluton and the associated dykes. This is another small, composite pluton (González Guillot *et al*. 2012), with dykes having a diverse range of compositions. The dykes emplaced in two main stages separated by an event of ductile deformation (Torres Carbonell *et al*. 2020).

A final remark on the contact aureole, while qualitative, can provide clues for further research. There is a significant difference in the extent and grade of the aureole around the Ushuaia pluton [>2 km from pluton margins (see Geological Setting); González Guillot *et al*. 2018] and those around the Trapecio and UPA dyke swarms. The aureole around the Kranck pluton-dyke system is also very poorly developed (González Guillot et al. 2012). Among the many factors that can control the extension of the aureole (Barton *et al*. 1991), magma volume (and associated advecting hydrothermal system) and injection rates (e.g. Annen 2011) may have played a major role. These factors should have been of different magnitude during the emplacement of the Trapecio and UPA (and Kranck) pluton-dyke systems, on the one hand, and of the Ushuaia pluton, on the other; while magma temperature, temperature contrast with the host-rock, depth of emplacement and host-rock composition are assumed to be similar. All the intrusions are small, although the Ushuaia pluton appears to have a volume an order of magnitude larger, according the outcrop area (González Guillot *et al*. 2018) and geophysical modelling (Peroni *et al*. 2009). Therefore, magma volume might have controlled the development of the aureole to some extent. The other factor is the intrusion rate, which along with the mode of emplacement, exerts a control on the cooling rate (Annen 2011; Blundy and Annen 2016). The small size of the plutons suggests fast cooling rates (de Saint Blanquat *et al*. 2011; Blundy and Annen 2016). However, high accretion rates were proposed for the Ushuaia pluton, that allowed low cooling rates and incomplete consolidation of previous batches of magma when new batches arrived (González Guillot *et al*. 2018). This favoured a high-temperature environment that led to country rock partial melting and its plastic deformation along pluton margins, in addition to the development of an extensive contact aureole. On the contrary, the injection rates should have been low in the Trapecio and UPA pluton-dyke systems, thus favouring fast dissipation of heat. The same is assumed for the Kranck pluton-dyke system. The strong deuteric alteration of the dykes, their fine-grained groundmasses and the breccia at Dos Lomos peninsula, suggests hydrothermal fluids escaping through the dykes, promoting further cooling.

The Ushuaia pluton is limited on its northeastern margin by a regional fault (Fig. 1b), and it was proposed that the emplacement of the pluton was controlled by this structure (González Guillot *et al*. 2018). We speculate that channelized magma tapping from below facilitated high injection rates in the Ushuaia pluton, whereas the lack of regional faults around the Trapecio and UPA dyke swarms hampered magma transport, leading to lower injection rates.

Conclusions

We characterized the field geology, petrography, geochemistry and geochronology of two Late Cretaceous dyke swarms in the Fuegian Andes: the Trapecio and the Ushuaia Peninsula (UPA) dyke swarms. The Trapecio dyke swarm belongs to the Fuegian Potassic Magmatism (FPM), a rear-arc suite in Tierra del Fuego (González Guillot *et al*. 2009). The dykes, emplaced at 74.56 Ma, are assumed to overly a small pluton, the Trapecio pluton, whose roof possibly lies *c*. 320 m below the Trapecio hill

area. Whole-rock trace element composition allows to distinguish this body form other plutons of the suite, including the neighbouring Ushuaia pluton.

On the other hand, the field and analytical data suggest the plugs and dykes at Ushuaia peninsula represent the cupola of another small pluton that lies mostly beneath the surface. The UPA have ages in the range 87.46-84.1 Ma, thus emplaced at least 7.6 Myr earlier than the Trapecio dyke swarm, and 3.7 Myr earlier than the oldest FPM rocks. The UPA dykes were affected by deformation associated with the closure of the Rocas Verdes basin, whereas the Trapecio dykes were not. The chronological data presented here allow to better constrain the age of this deformation in the study area, to the interval bracketed by the emplacement of the UPA dyke swarm (87.5-84.1 Ma) and the Ushuaia pluton and Trapecio dyke swarm (77.5-71 Ma).

Both suites are easily distinguished by geochemistry. The FPM (including the Trapecio dyke swarm) follow mildly alkaline and ferriferous trends, whereas the UPA dyke swarm have high-K calc-alkaline and magnesian affinities. However, distinguishing these suites by whole-rock composition based on mobile elements may be not fully reliable, due to intense alteration in many dykes. However, K_2O content in amphibole allows to distinguish clearly these two suites from each other, as well as from plutons with medium K calc-alkaline composition of the Fuegian batholith.

We propose that the dykes at the Trapecio hill area and the Ushuaia peninsula represent a protracted history of dyke injection at the roof of small plutons emplaced in the shallow crust, most of them fed from mid/lower-crustal reservoirs. Low injection rates, small magma volume and release of hydrothermal fluids through dykes, allowed fast dissipation of heat, and were probably the main factors controlling the development of a small contact aureole.

Acknowledgements

MGG acknowledges Rogelio Acevedo and Hernán De Ángelis (CADIC-CONICET), Mariano Fehrmann, Luis Jara Poza for field assistance; and Andrea Coronato (CADIC-CONICET) for discussion on glacial activity in the region. Miguel Barbagallo and Leandro Remón (CADIC-CONICET) contributed with thin section preparation. Nilson Francisquini Botelho and Ricardo Lívio (Brasilia University), Manuel Demartis (Río Cuarto University), Alina Guereschi (CICTERRA-CONICET) are thanked for microprobe assistance and facilities; and Miguel Basei (São Paulo University) for assistance with LA-ICP-MS geochronology. We also acknowledge the Base Naval Ushuaia for allowing access to the UPA outcrops. We greatly appreciate editorial handling by Lorenzo Fedele and reviewing by himself, John Bartley, Jiří Žák and an anonymous reviewer that helped to improve this paper.

Funding

LA-ICP-MS geochronology at La.Te.Andes was financed by a subsidy of La.Te.Andes S.A. and CONICET for CONICET based research projects. Additional funds were obtained from FONCyT (PICT 2010-1937, MGG; PICT 2015-2982 and 2019-1541, PTC, MGG and SC) and Consejo Federal de Inversiones (CONICET Resolution 1502 2005/09/16; R. Acevedo).

References

Acevedo, R., Linares, E., Ostera, H. and Valín-Alberdi, M. 2002. La Hornblendita Ushuaia (Tierra del Fuego): Geoquímica y Geocronología. Revista Asociación Geológica Argentina, 57(2), 133-142.

Alasino, P., Larrovere, M., Rocher, S., Dahlquist, J., Basei, M., Memeti, V., Paterson, S., Galindo, C., Macchioli Grande, M., da Costa, M. 2017. Incremental growth of an upper crustal, A-type pluton, Argentina: evidence of a re-used magma pathway. Lithos, doi:10.1016/j.lithos.2017.04.013

Allmendinger, R., Cardozo, N. and Fisher, D. 2013. Structural geology algorithms: Vectors and tensors in structural geology. Cambridge University Press, England.

Annen, C., 2011. Implications of incremental emplacement of magma bodies for magma differentiation, thermal aureole dimensions and plutonism–volcanism relationships. Tectonophysics, 500, 3-10.

Barbeau, D., Gombosi, D., Zahid, K., Bizimis, M., Swanson-Hysell, N., Valencia, V. and Gehrels, G. 2009. U-Pb zircon constraints on the age and provenance of the Rocas Verdes basin-fill, Tierra del Fuego, Argentina. Geochemistry, Geophysics, Geosystems, 10, Q12001, doi:10.1029/2009GC002749

Barnett, W., Kurszlaukis, S., Tait, M. and Dirks, P. 2011. Kimberlite wall-rock fragmentation processes: Venetia K08 pipe development. Bulletin of Volcanology, doi:10.1007/s00445-011-0499-3

Bartley, J., Glazner, A. and Coleman, D. 2018. Dike intrusion and deformation during growth of the Half Dome pluton, Yosemite National Park, California. Geosphere, 14(3), 1283-1297, doi:10.1130/GES01458.1

Barton, M., Staude, J., Snow, E., Johnson, D. 1991. Aureole systematics. In: Kerrick, D. (ed) Contact Metamorphism. Reviews in Mineralogy, 26, 723-847.

Blundy, J. and Annen, C. 2016. Crustal magmatic systems from the perspective of heat transfer. Elements, 12, 115-120.

Bonechi, B., Perinelli, C., Gaeta, M., Tecchiato, V. and Granati, S. 2017. Experimental constraints on amphibole stability in primitive alkaline and calc-alkaline magmas. Periodico di Mineralogia, 86, 231-245, doi:10.2451/2017PM735

Calderón, M., Fosdick, J., Warren, C., Massonne, H.-J., Fanning, M., Fadel Cury, L., Schwanethal, J., Fonseca, P., Galaz, G., Gaytán, D., Hervé, F. 2012. The low-grade Canal de las Montañas Shear Zone and its role in the tectonic emplacement of the Sarmiento Ophiolitic Complex and Late Cretaceous Patagonian Andes orogeny, Chile. Tectonophysics, 524-525, 165-185.

Calderón, M., Hervé, F., Fuentes, F., Fosdick, J., Sepúlveda, F. and Galaz, G. 2016. Tectonic Evolution of Paleozoic and Mesozoic Andean Metamorphic Complexes and the Rocas Verdes Ophiolites in Southern Patagonia. In: Ghiglione, M. (ed) Geodynamic Evolution of the Southernmost Andes: Connections with the Scotia Arc. Springer International Publishing, 7-36.

Caminos, R. 1980. Cordillera Fueguina. En Geología Regional Argentina. Academia Nacional de Ciencias, Córdoba, 2, 1463-1501.

Cao, S., Torres Carbonell, P. and Dimieri, L. 2018. Structural and petrographic constraints on the stratigraphy of the Lapataia Formation, with implications for the tectonic evolution of the Fuegian Andes. Journal of South American Earth Sciences, 84, 223-241.

Cao, S., Torres Carbonell, P., Sánchez, N., Bordese, S. and Dimieri, L. 2023. Thrust tectonics in the Fuegian Andes central belt: a detailed geometric-kinematic analysis and new thermochronological constraints. Tectonophysics, doi.org/10.1016/j.tecto.2023.229966

Cashman, K. and Blundy, J. 2000. Degassing and crystallization of ascending andesite and dacite. Philosophical Transactions of the Royal Society of London, A 358, 1487-1513.

Cox, K., Bell., J. and Pankhurst, R. 1979. The interpretation of igneous rocks. London, Allen and Unwin.

Cunningham, W.D. 1995. Orogenesis at the southern tip of the Americas: the structural evolution of the Cordillera Darwin metamorphic complex, southernmost Chile. Tectonophysics, 244, 197-229.

de Saint Blanquat, M., Horsman, E., Habert, G., Morgan, S., Vanderhaeghe, O., Law, R. and Tikoff, B. 2011. Multiscale magmatic cyclicity, duration of pluton construction, and the paradoxical relationship between tectonism and plutonism in continental arcs. Tectonophysics, 500, 20-33.

Delaney, P. and Pollard, D. 1981. Deformation of Host Rocks and Flow of Magma during Growth of Minette Dikes and Breccia-bearing Intrusions near Ship Rock, New Mexico. Geological Survey Professional Paper, 1202, Washington.

Erdman, S., Martel, C., Pichavant, M. and Kushnir, A. 2014. Amphibole as an archivist of magmatic crystallization conditions: problems, potential, and implications for inferring magma storage prior to the paroxysmal 2010 eruption of Mount Merapi, Indonesia. Contributions to Mineralogy and Petrology, 167, 1016, doi:10.1007/s00410-014-1016-4

Fiedrich, A., Bachmann, O., Ulmer, P., Deering, C., Kunze, K. and Leuthold, J. 2017. Mineralogical, geochemical, and textural indicators of crystal accumulation in the Adamello Batholith (Northern Italy). American Mineralogist, 102, 2467-2483.

Fiske, R., Hopson, C., Waters, A. 1963. Geology of Mount Rainier National Park, Washington. US Geological Survey Professional Paper, 444.

Fildani, A., Cope, T., Graham, S. and Wooden, J. 2003. Initiation of the Magallanes foreland basin: Timing of the southernmost Patagonian Andes orogeny revised by detrital zircon provenance analysis. Geology, 31, 1081-1084.

GERM Database (www.earthref.org), data contribution by Nielsen, R. [Last accessed November 2023].

Ghiglione, M., Quinteros, J., Yagupsky, D., Bonillo-Martínez, P., Hlebszevtich, J., Ramos, V., Vergani, G., Figueroa, D., Quesada, S. and Zapata, T. 2010. Structure and tectonic history of the foreland basins of southernmost South America. Journal of South American Earth Sciences, 29, 262-277.

Giusti, R., Colombo, G., Pandeli, E., Elter, F., Casalini, M., Orti, L. 2023. The plutonic-dyke system and host Ligurian successions of the island of Montecristo (Tuscan archipelago, Italy): new stratigraphic, petrographic and structural data. Ofioliti, 48(1), 47-73, doi:10.4454/ofioliti.v48i1.561

Glazner, A., McNutt, S. 2021. Relationship between dike injection and b-value for volcanic earthquake swarms. Journal of Geophysical Research: Solid Earth, 126, 10.1029/2020JB021631.

Glazner, A., Bartley, J., Coleman, D., Gray, W. and Taylor, R. 2004. Are plutons assembled over millions of years by amalgamation from small magma chambers? GSA Today, 14(4/5), 4-11.

González Guillot, M. 2016. Magmatic evolution of the southernmost Andes and its relation with subduction processes. In: Ghiglione, M. (ed) Geodynamic Evolution of the Southernmost Andes: Connections with the Scotia Arc. Springer International Publishing, 37-74.

González Guillot, M., Escayola, M., Acevedo, R., Pimentel, M., Seraphim, G., Proenza, J. and Schalamuk, I. 2009. The Plutón Diorítico Moat: Mildly alkaline monzonitic magmatism in the Fuegian Andes of Argentina. Journal of South American Earth Sciences, 28, 345-359.

González Guillot, M., Escayola, M. and Acevedo, R. 2011. Calc-alkaline rear-arc magmatism in the Fuegian Andes: implications for the mid-Cretaceous tectonomagmatic evolution of southernmost South America. Journal of South American Earth Sciences, 31, 1-16.

González Guillot, M., Prezzi, C., Acevedo, R. and Escayola, M. 2012. A comparative study of two rear-arc plutons and implications for the Fuegian Andes tectonic evolution: mount Kranck Pluton and Jeu-Jepén Monzonite, Argentina. Journal of South American Earth Sciences, 38, 71-88.

González Guillot, M., Ghiglione, M., Escayola, M., Martins Pimentel, M., Mortensen, J. and Acevedo, R. 2018. Ushuaia pluton: Magma diversification, emplacement and relation with regional tectonics in the southernmost Andes. Journal of South American Earth Sciences, 88, 497-519, doi.org/10.1016/j.jsames.2018.10.001

Gorini, A., Ridolfi, F., Piscaglia, F., Taussi, M. and Renzulli, A. 2018. Application and reliability of calcic amphibole thermobarometry as inferred from calc-alkaline products of active geothermal areas in the Andes. Journal of Volcanology and Geothermal Research, 358, 58-76, doi.org/10.1016/j.jvolgeores.2018.03.018

Guo, Ch-L., Wilde, S., Henderson, R., Li, Q-L. and Yin, B. 2020. Cogenetic dykes the key to identifying diverse magma batches in the assembly of granitic plutons. Journal of Petrology, 61(11-12), egaa105, doi.org/10.1093/petrology/egaa105

Hervé, M., Suárez, M. and Puig, A. 1984. The Patagonian Batholith south of Tierra del Fuego, Chile. Timing and tectonic implications. Journal of the Geological Society, London, 141(5), 909-917.

Hibbard, M.J. 1995. Petrography to Petrogenesis. Prentice Hall, New Jersey.

Hoyer, L. and Watkins, M. 2016. Breccia formation during intrusion of a dolerite sill: an example from Sheffield Beach, KwaZulu-Natal North Coast, South Africa. South African Journal of Geology, 119.4, 663-676, doi:10.2113/gssajg.119.4.663

Isla, F., Bujalesky, G. and Coronato, A. 2001. Procesos estuarinos en el Canal Beagle, Tierra del Fuego. Revista de la Asociación Geológica Argentina, 54 (4), 307-318.

Innocenti, F., Westerman, D., Rocchi, S., Tonarini, S. 1997. The Montecristo monzogranite (Northern Tyrrhenian Sea, Italy): a collisional pluton in an extensional setting. Geological Journal, 32, 131-151.

Jackson, M. and Pollard, D. 1988. The laccolith-stock controversy: New results from the southern Henry Mountains, Utah. Geological Society of America Bulletin, 100, 117-139.

Jamtveit, B., Svensen, H., Podladchikov, Y. and Planke, S. 2004. Hydrothermal vent complexes associated with sill intrusions in sedimentary basins. In: Breitkreuz, C. and Petford, N. (eds) Physical Geology of High-Level Magmatic Systems. Geological Society of London, Special Publications, 234, 233-241.

Janousek, V., Farrow, C. and Erban, V. 2006. Interpretation of whole-rock geochemical data in igneous geochemistry: introducing Geochemical Data Toolkit (GCDkit). Journal of Petrology, 47(6), 1255-1259, doi:10.1093/petrology/egl013

Klepeis, K., Betka, P., Clarke, G., Fanning, M., Hervé, F., Rojas, L., Mpodozis, C. and Thomson, S. 2010. Continental underthrusting and obduction during the Cretaceous closure of the Rocas Verdes rift basin, Cordillera Darwin, Patagonian Andes. Tectonics, 29, TC3014.

Kohn, M., Spear, F., Harrison, T. and Dalziel, I. 1995. $^{40}Ar/^{39}Ar$ geochronology and P-T-t paths from the Cordillera Darwin metamorphic complex, Tierra del Fuego, Chile. Journal of Metamorphic Geology, 13, 251-270.

Krawczynski, M., Grove, T. and Behrens, H. 2012. Amphibole stability in primitive arc magmas: effects of temperature, H_2O content, and oxygen fugacity. Contributions to Mineralogy and Petrology, doi:10.1007/s00410-012-0740-x

Leake, B., Woolley, A., Arps, C., Birch, W., Gilbert, M., Grice, J., Hawthorne, F., Kato, A., Kisch, H., Krivovichev, V., Linthout, K., Laird, J., Mandarino, J., Maresch, W., Nickel, E., Rock, N., Schumacher, J., Smith, D., Stephenson, N., Ungaretti, L., Whittaker, E., Youzhi, G. 1997. Nomenclature of amphiboles: Report of the Subcommittee on Amphiboles of the IMA, Commission on New Minerals and Mineral Names. Canadian Mineralogist, 35, 219-246.

Leuthold, J., Müntener, O., Baumgartner, L. and Putlitz, B. 2014. Petrological constraints on the recycling of mafic crystal mushes and intrusion of braided sills in the Torres del Paine Mafic Complex (Patagonia). Journal of Petrology, 55, 917-949.

Lorenz, V. and Kurszlaukis, S. 2007. Root zone in the phreatomagmatic pipe emplacement model and consequences for the evolution of maar-diatreme volcanoes. Journal of Volcanology and Geothermal Research, 159, 4-32.

Mahan, K., Bartley, J., Coleman, D., Glazner, A. and Carl, B. 2003. Sheeted intrusion of the synkinematic McDoogle pluton, Sierra Nevada, California. Geological Society of America Bulletin, 115(12), 1570-1582.

Maloney, K., Clarke, G., Klepeis, K., Fanning, C. and Wang, W. 2011. Crustal growth during back-arc closure: Cretaceous exhumation history of Cordillera Darwin, southern Patagonia. Journal of Metamorphic Geology, doi:10.1111/j.1525-1314.00934.x

Martín, G., González Guillot, M., Escayola, M. 2023. Resultados geotermobarométricos preliminares en la Formación Lemaire, Andes Fueguinos Argentinos. 14 Congreso de Mineralogía, Petrología Ígnea y Metamórfica, y Metalogénesis (MINMET), Bahía Blanca, Argentina, Abstracts, 291-293.

McAtamney, J., Klepeis. K., Mehrtens, C., Thomson, S., Betka, P., Rojas, L., Snyder, S. 2011. Along-strike variability of back-arc basin collapse and the initiation of sedimentation in the Magallanes foreland basin, southernmost Andes (53–54.5°S). Tectonics, 30, TC5001, doi:10.1029/2010TC002826

Menichetti, M., Lodolo, E. and Tassone, A. 2008. Structural geology of the Fuegian Andes and Magallanes fold-and-thrust belt- Tierra del Fuego island. Geologica Acta, 6, 19-42.

Middlemost, E. 1994. Naming materials in magma/igneous rock system. Earth Science Reviews, 37, 215-224.

Molina, J., Scarrow, J., Montero, P. and Bea, F. 2009. High-Ti amphibole as a petrogenetic indicator of magma chemistry: Evidence for mildly alkalic-hybrid melts during evolution of Variscan basic-ultrabasic magmatism of Central Iberia. Contributions to Mineralogy and Petrology, 158, 69-98.

Molina, J., Cambeses, A., Moreno, J., Morales, I., Montero, P. and Bea, F. 2021. A reassessment of the amphibole-plagioclase NaSi-CaAl exchange thermometer with applications to igneous and high-grade metamorphic rocks. American Mineralogist, 106, 782-800, doi.org/10.2138/am-2021-7400

Muller, V., Calderón, M., Fosdick, J., Ghiglione, M., Cury, L., Massonne, H.-J., Fanning, M., Warren, C., Ramírez de Arellano, C., Sternai, P. 2021. The closure of the Rocas Verdes Basin and early tectono-metamorphic evolution of the Magallanes Fold-and-Thrust Belt, southern Patagonian Andes (52–54◦S). Tectonophysics, 798, 228686.

Nelson, E., Dalziel, I. and Milnes, A. 1980. Structural geology of the Cordillera Darwin - Collisional-style orogenesis in the southernmost Chilean Andes. Eclogae Geologicae Helvetiae, 73, 727-751.

Olivero, E., and Martinioni, D. 1996a. Sedimentología de las Formaciones Lemaire y Yahgan (Jurásico-Cretácico) en Tierra del Fuego. Actas XIII Congreso Geológico Argentino y III Congreso de Exploración de Hidrocarburos, 2, 45-59.

Olivero, E., and Martinioni, D. 1996b. Late Albian inoceramid bivalves from the Andes of Tierra del Fuego: Age implications for the closure of the Cretaceous Marginal Basin. Journal of Paleontology, 70, 272-274.

Olivero, E. and Malumián, N. 2008. Mesozoic-Cenozoic stratigraphy of the Fuegian Andes, Argentina. Geologica Acta, 6, 5-18.

Parmigiani, A., Degruyter, W., Leclaire, S., Huber, C. and Bachmann, O. 2017. The mechanics of shallow magma reservoir outgassing. Geochemistry Geophysics Geosystems, 18, 2887-2905, doi:10.1002/2017GC006912

Peroni, J., Tassone, A., Menichetti, M. and Cerredo, M. 2009. Geophysical modeling and structure of Ushuaia Pluton, Fuegian Andes, Argentina. Tectonophysics, 476, 436-449.

Peroni, J., Tassone, A. and Vilas, J. 2016. Modelado magnético del plutón Trapecio, Tierra del Fuego, Argentina. Latinmag Letters, 6, Special Issue, A11, 1-4.

Pitcher, W. 1993. The Nature and Origin of Granite. Blackie Academic, Glasgow.

Pitcher, W., Bussell, M.A. 1985. Andean dyke swarms: andesite in synplutonic relationship with tonalite. In: Pitcher, W., Atherton, M., Cobbing, E.J. and Beckinsale, R. (eds) Magmatism at a plate edge: the Peruvian Andes. Blackie, 103-107.

Platten, I.M. 1984. Fluidized mixtures of magma and rock in a late Caledonian breccia dyke and associated breccia pipes in Appin, Scotland. Geological Journal, 19(3), 209-226, doi.org/10.1002/gj.3350190302

Poblete, F., Roperch, P., Arriagada, C., Ruffet, G., Ramírez de Arellano, C., Hervé, F., Poujol, M. 2016. Late Cretaceous–early Eocene counterclockwise rotation of the Fuegian Andes and evolution of the Patagonia-Antarctic Peninsula system. Tectonophysics, 668-669, 15-34.

Putirka, K. 2008. Thermometers and barometers for volcanic systems. In: Putirka, K. and Tepley, F. (eds) Minerals, Inclusions and Volcanic Processes. Reviews in Mineralogy and Geochemistry, 69, 61-120, https://doi.org/10.2138/rmg.2008.69.3

Putirka, K. 2016. Amphibole thermometers and barometers for igneous systems and some implications for eruption mechanisms of felsic magmas at arc volcanoes. American Mineralogist, 101, 841-858.

QGIS.org 2021. QGIS Geographic Information System. QGIS Association. www.qgis.org/

Rabassa, J., Coronato, A., Bujalesky, G., Roig, C., Salemme, M., Meglioli, A., Heuser, C., Gordillo, S., Borromei, A. and Quatrocchio, M. 2000. Quaternary of Tierra del Fuego, Southernmost South America: un updated review. Quaternary International, 68-71, 217-240.

Rapalini, A., Peroni, J., Luppo, T., Tassone, A., Cerredo, M., Esteban, F., Lippai, H., Vilas, J. 2015. Palaeomagnetism of Mesozoic magmatic bodies of the Fuegian Cordillera: implications for the formation of the Patagonian Orocline. Geological Society, London, Special Publications, 425 http://dx.doi.org/10.1144/sp425.3

Rhodes, E., Barker, A., Burchardt, S., Hieronymus, C., Rousku, S., McGarvie, D., Mattsson, T., Schmiedel, T., Ronchin, E., Witcher, T. 2021. Rapid assembly and eruption of a shallow silicic magma reservoir, Reyðarártindur pluton, southeast Iceland. Geochemistry, Geophysics, Geosystems, 10.1029/2021GC009999.

Rickwood, P. 1989. Boundary lines between petrologic diagrams which use oxides of major and minor elements. Lithos, 22, 247-263.

Ridolfi, F. 2021. Amp-TB2: An Updated Model for Calcic Amphibole Thermobarometry. Minerals, 11, 324, doi.org/10.3390/min11030324

Ridolfi, F. and Renzulli, A. 2012. Calcic amphiboles in calc-alkaline and alkaline magmas: thermobarometric and chemometric empirical equations valid up to 1,130 °C and 2.2 GPa, Contributions to Mineralogy and Petrology, 163, 877-895.

Ridolfi, F., Renzulli, A. and Puerini, M., 2010. Stability and chemical equilibrium of amphibole in calc-alkaline magmas: an overview, new thermobarometric formulations and application to subduction-related volcanoes. Contributions to Mineralogy and Petrology, 160, 45-66.

Rock, N.M.S. 1991. Lamprophyres. Van Nostrand Reinhold, New York.

Schofield, N.J., Brown, D.J., Magee, C. and Stevensen, C.T. 2012. Sill morphology and comparison of brittle and non-brittle emplacement mechanisms. Journal of the Geological Society, London, 169, 127-141.

SEGEMAR. 1998. Levantamiento geofísico aéreo, magnetometría área de Tierra del Fuego. Proyecto PASMA. Hojas 5569-II, 5566-I, 5566-II. Escala 1:250000.

SERNAGEOMIN. 2003. Mapa Geológico de Chile. Servicio Nacional de Geología y Minería, Publicación Geológica Digital, 4 (CD-ROM, versión 1.0).

Sparks, R., Baker, L., Brown, R., Field, M., Schumacher, J., Stripp, G. and Walters, A. 2006. Dynamic constraints on kimberlite volcanism. Journal of Volcanology and Geothermal Research, 155, 18-48.

Stern, C., de Wit, M. 2003. Rocas Verdes ophiolites, southernmost South America: remnants of progressive stages of development of oceanic-type crust in a continental margin back-arc basin. Geological Society, London, Special Publications, 218, 665-683.0305-8719/03/$15

Suárez, M., Hervé, M. and Puig, A. 1985. Hoja Isla Hoste e islas adyacentes, XII Región. Carta Geológica de Chile 1:250.000. Servicio Nacional de Geología y Minería, Chile, 65.

Suárez, M. Hervé, M. and Puig, A. 1987. Cretaceous diapiric plutonism in the southern cordillera, Chile. Geological Magazine, 124, 569-575.

Sun, S.S. and McDonough, W.F. 1989. Chemical and isotopic systematics of oceanic basalts: implications for mantle composition and processes. In: Saunders, A. and Norry, M. (eds) Magmatism in Ocean Basins. Geological Society, London, Special Publications, 42, 313-345.

Torres Carbonell, P. and Dimieri, L. 2013. Cenozoic contractional tectonics in the Fuegian Andes, southernmost South America: a model for the transference of orogenic shortening to the foreland. Geologica Acta, 11, 359-370.

Torres Carbonell, P., Dimieri, L., Olivero, E., Bohoyo, F. and Galindo-Zaldívar, J. 2014. Structure and tectonic evolution of the Fuegian Andes (southernmost South America) in the framework of the Scotia Arc development. Global and Planetary Change, 123, B, 174-188.

Torres Carbonell, P., Rodríguez Arias, L. and Atencio, M. 2017. Geometry and kinematics of the Fuegian thrust-fold belt, southernmost Andes. Tectonics, 36, 33-50.

Torres Carbonell, P., Cao, S., González Guillot, M., Mosqueira, V., Dimieri, L., Duval, F. and Scaillet, S. 2020. The Fuegian thrust-fold belt: From arc-continent collision to thrust-related deformation in the southernmost Andes. Journal of South American Earth Sciences, 102, 102678, doi.org/10.1016/j.jsames.2020.102678

Torres García, M., Calderón, M., Ramírez de Arellano, C., Hervé, F., Opitz, J., Theye, T., Fanning, C., Pankhurst, R., González Guillot, M., Fuentes, F., Babinski, M. 2020. Trace element composition of amphibole and petrogenesis of hornblendites and plutonic suites of distinct Cretaceous magmatic arcs developed in the Fuegian Andes, southernmost South America. Lithos, doi.org/10.1016/j.lithos.2020.105656

Turrillot, P., Faure, M., Martelet, G., Chen, Y., Augier, R. 2011. Pluton-dyke relationships in a Variscan granitic complex from AMS and gravity modelling. Inception of the extensional tectonics in the South Armorican Domain (France). Journal of Structural Geology, 33, 1681-1698.

Uchida, E., Endo, S. and Makino, M. 2007. Relationship Between Solidification Depth of Granitic Rocks and Formation of Hydrothermal Ore Deposits. Resource Geology, 57(1), 47-56, doi:10.1111/j.1751-3928.2006.00004.x

Valentine, G.A., Graettinger, A.H. and Sonder, I. 2014. Explosion depths for phreatomagmatic eruptions. Geophysical Research Letters, 41, 3045-3051.

Velásquez, R. Bastías, J., Salazar, E., Poblete, F., González Guillot, M., Chew, D., Peña, M., Tapia, F., Ramírez, A. and Drakou, F. 2023. Magmatic arc evolution during the tectonic closure of the Rocas Verdes basin: insights from Cretaceous-earliest Paleocene intrusive rocks of Navarino Island (55°S), Fuegian Andes. Journal of the Geological Society, London, doi.org/10.1144/jgs2022-163

Vermeesch, P. 2018. IsoplotR: a free and open toolbox for geochronology. Geoscience Frontiers, 9, 1479-1793, doi:10.1016/j.gsf.2018.04.001

Wallrich, B., Miller, C., Gualda, G., Miller, J., Hinz, N., Faulds, J. 2023. Volcano-pluton connection: Perspectives on material and process linkages, Searchlight pluton and Highland Range volcanic sequence, Nevada, USA. Earth-Sciences Reviews, 238, 104361.

White, J., McPhie, J. and Skilling, I. 2000. Peperite: a useful genetic term. Bulletin of Volcanology, 62, 65-66.

Whitney, D. and Evans, B. 2010. Abbreviations for names of rock-forming minerals. American Mineralogist, 95, 185-187, doi.org/10.2138/am.2010.3371

Wilson, L. and Head, J. 2003. Diatremes and kimberlites 2: an integrated model of the ascent and eruption of kimberlitic magmas and the production of crater, diatreme, and hypabyssal facies. International Kimberlite Conference: Extended Abstracts, 8, https://doi.org/10.29173/ikc3153

Wilson, L. and Head, J. 2007. An integrated model of kimberlite ascent and eruption. Nature, 447, doi:10.1038/nature05692

Yoshinobu, A., Fowler Jr., T.K., Paterson, S., LLambías, E., Tickyj, H., Sato, A. 2003. A view from the roof: magmatic stoping in the shallow crust, Chita pluton, Argentina. Journal of Structural Geology, 25, 1037-1048.

Zuck, F. and González Guillot, M. 2022. Petrografía de facies de borde en el plutón Ushuaia, Tierra del Fuego, Argentina. 21 Congreso Geológico Argentino, Puerto Madryn, Argentina, Abstracts, 1515-1516.

Figure captions

Fig. 1. (a) Regional geological map of Tierra del Fuego (modified from González Guillot *et al.* 2018). Numbers refer to plutons of the Fuegian Potassic Magmatism: (1) Ushuaia, (2) Moat, (3) Jeu-Jepén, (4) Kranck. Magenta star indicates the Trapecio dyke swarm. SR and C are Santa Rosa and Castores plutons. BCFZ, Beagle Channel fault zone; MFFZ, Magallanes Fagnano fault zone. Based on regional and local maps presented in Suárez *et al.* (1985), SERNAGEOMIN (2003), Olivero and Malumián (2008), González Guillot *et al.* (2009), Torres Carbonell *et al.* (2020), Velásquez *et al.* (2023). (b) Satellite image (Google, © 2023 Airbus/CNES Airbus/Maxar Technologies) with location of outcrops of UPA and Trapecio dyke swarms and the Ushuaia pluton (UP) (red lines). The location of sample MTC298B (UP, dated by Ar-Ar in this work) and Fig. 2 are indicated. DL is Dos Lomos peninsula. The aeromagnetic anomalies over UP and Trapecio dyke swarm are shown (yellow lines, from reduced to the pole chart, SEGEMAR 1998). The trace of the profile of Fig. 13 is also shown.

Fig. 2. (a) Topographic and geological map of the Trapecio hill area with location of analysed samples. The rectangle shows the location of figure b. (b) Satellite image (Google, © 2023 Airbus) showing folded strata (one depicted with yellow line) cross-cut by rectilinear dykes (width of image 140 m). (c) Lower hemisphere equal-area projection of dioritoid (n: 40) and lamprophyre (n: 12) dykes (same color key as in a), and mean attitude of the slaty cleavage in the host-rock for comparison (thick blue line). (d) Planes for the slaty cleavage (n: 32) and rose diagrams for the dip direction of the dykes (10° groups, same color key as in a, largest petal 25 %).

Fig. 3. Representative field photographs of the investigated Trapecio dykes. (a) 1.5 m thick dioritoid dyke (sample TR59) crosscutting strata and slaty cleavage (red lines) of the Yahgan Fm. Equal area projection shows tectonic foliation (red) and dyke (black) orientations and mean attitudes (dip direction/dip). Other dykes are seen in the background (indicated by black arrows). Looking southeast. (b) Small laccolithic body located at the southeast of the mapped area (partly outlined by white dashed line). Other dykes and sills are seen in the background (indicated by black arrows). (c) Dioritoid dyke

with oriented, flattened mafic microgranular enclaves (MME). (d) Angular mafic and ultramafic enclaves in dioritoid dyke.

Fig. 4. (a) Geological cross-sections of the UPA dyke swarm at the northern quarry (three benches, the lower and middle ones are split). Modified from González Guillot *et al*. (2011). (b) Plan view of the dyke and breccia at Dos Lomos peninsula. The inset shows the eastern tip of the Ushuaia peninsula, with location of the northern quarry (Q) and the dyke at Dos Lomos peninsula (DL). (c-d) Lower hemisphere equal-area projections for the attitude of the UPA dykes and foliation in the host-rock. (c) Leucocratic (andesite-dacite, n: 9) and lamprophyre dykes (n: 9), along with mean attitude of the metamorphic foliation in the host-rock (thick blue line). (d) Planes for the foliation in the host-rock (n: 8) and rose diagrams for the dip direction of the dykes (10° groups, same color key as in c, largest petal 57 %).

Fig. 5. (a) Field photograph of a UPA andesite dyke with sharp contacts, the stratification of host-rock is indicated (notebook is 16 cm wide). (b) Magnification of the contact on a rock slice showing no chilled margin at the contact with the slate (sl) country rock. The dyke is 6 cm thick and contains small, angular slate xenoliths. Thin quartz veinlets (v) cross-cut the host-rock. Note also the high phenocryst content. Pl, plagioclase; Hbl, hornblende; Py, pyrite.

Fig. 6. Heterobreccia on andesite dyke sides at Dos Lomos peninsula. (a) Field photograph and line drawing of outcrop, looking SW (hammer for scale); p and s denote pelite and sandstone, respectively (only few igneous and sedimentary clasts are depicted within the breccia as example). (b) Detail of the contact between the dyke and the breccia. Note sedimentary clasts and protrusions within the dyke (black arrows) and igneous clasts and protrusions within the breccia (white arrows). (c) Plane polarized light photomicrograph of deformed, flattened igneous clast (delimited by white dashed line) set in a sandstone-sized matrix resulted from comminution of sedimentary host and dyke. The andesite clast is porphyritic with altered plagioclase phenocrysts (Pl) and allanite (Aln) microphenocrysts in a very fine grained groundmass. Note indentation of clast (arrow) against pelite (p) fragment.

Fig. 7. (a) Classification of the analysed amphibole crystals from the Trapecio dyke swarm (left panel) and UPA (right panel), following Leake *et al*. (1997). (b) K vs. Si diagram with additional data from other FPM plutons (unpublished data) and the Fuegian batholith (FB; Torres García *et al*. 2020) for comparison. Left panel shows magnesiohastingsite, pargasite, ferropargasite and edenite only [$(Na+K)_A \geq 0.50$]. Right panel includes all amphiboles. The thick blue lines represent limits for medium-K calc-alkaline (MK), high-K calc-alkaline (HK) and shoshonitic/monzonitic (SH-M) mildly alkaline series. Coordinates (x,y) are: lower curve (5.5,0.144), (6.5,0.128), (7.65,0.0); upper curve (5.5,0.254), (6.3,0.213), (7.0,0.103). Abbreviations: gmass, groundmass; µphe, microphenocryst; MME, mafic microgranular enclave. Plutons: JJP, Jeu-Jepén; MP, Moat; UP, Ushuaia; KP, Kranck.

Fig. 8. Classification of the analysed (a) plagioclase and (b) biotite crystals from the Trapecio and UPA dyke swarms. Abbreviations: MME, mafic microgranular enclave; pheno, phenocryst. Inclusion (incl.) is plagioclase microphenocryst included in alkali feldspar and biotite included in hornblende. In (b) biotite from FPM plutons (Jeu-Jepén, JJP; Moat, MP; and Kranck, KP; unpublished data) are plotted for comparison.

Fig. 9. Whole-rock major and minor oxide composition of Trapecio dyke swarm (anhydrous basis). (a) Total alkali vs. silica (TAS) from Middlemost (1994) with line dividing fields from Cox *et al*. (1979). Also plotted are the compositional fields for the primary amphiboles of Trapecio and UPA dyke swarms, and Ushuaia pluton (encircled, same colour key as whole-rock). (b) K_2O vs. SiO_2 diagram (modified from Rickwood 1989). (c-i) Selected oxide vs. SiO_2 diagrams. (a-b) Also show for comparison data for:

the UPA dyke swarm (González Guillot *et al*. 2011); FPM plutons: Ushuaia [ultramafic-mafic (UMM) and intermediate (I) sections; Acevedo *et al*. 2002; González Guillot *et al*. 2018], Moat (MP, González Guillot *et al*. 2009), Jeu-Jepén (JJP, González Guillot *et al*. 2012), Kranck (KP, González Guillot *et al*. 2012); and the Fuegian batholith (Suárez *et al*. 1985; Torres García *et al*. 2020).

Fig. 10. (a) CaO/Al_2O_3 ratio and selected compatible and incompatible trace elements (b-d) abundancies and (e-i) ratios against silica for the Trapecio dyke swarm (anhydrous basis). Data for the UPA dyke swarm (González Guillot *et al*. 2011) and the Ushuaia pluton (Acevedo *et al*. 2002; González Guillot *et al*. 2018) are plotted for comparison. UP UMM and I refer to the ultramafic-mafic and intermediate sections of the Ushuaia pluton. In (e) qualitative trends of clinopyroxene (CF Cpx) and hornblende (CF Amp) fractionation are shown.

Fig. 11. (a) Primitive mantle and (b) CI chondrite normalized (Sun and McDonough 1989) diagrams for the Trapecio dyke swarm samples, compared with the UPA dyke swarm (left panel, González Guillot *et al*. 2011) and the Ushuaia pluton (UP, right panel, González Guillot *et al*. 2018). UP UMM and I refer to the ultramafic-mafic and intermediate sections of the Ushuaia pluton.

Fig. 12. Radiometric ages of the analysed samples from the Trapecio (a-b) and UPA dyke swarms (c-g), and the Ushuaia pluton (UP) (h). (a, c, e) Wetherill concordia ages with all concordant data (100 ± 10 %), the insets show the radial plots with zircon 206/238 ages. (b, d, f) Weighted mean zircon 206/238 ages of the filtered data (green + grey bars; green bars alone used for preferred crystallization age, white bars not included). (g, h) Hornblende Ar-Ar weighted mean ages.

Fig. 13. Schematic geological cross-section across the UPA dyke swarm, the Ushuaia pluton and the Trapecio dyke swarm (location of profile in Fig. 1b), based on field (González Guillot *et al*. 2011, 2018, this work) and geophysical (Peroni *et al*. 2009, 2016) evidence. Folding and foliation of the Yahgan Formation are schematically depicted, but we emphasize that these structures are less developed near the UPA, as explained in the text.

Figure 1

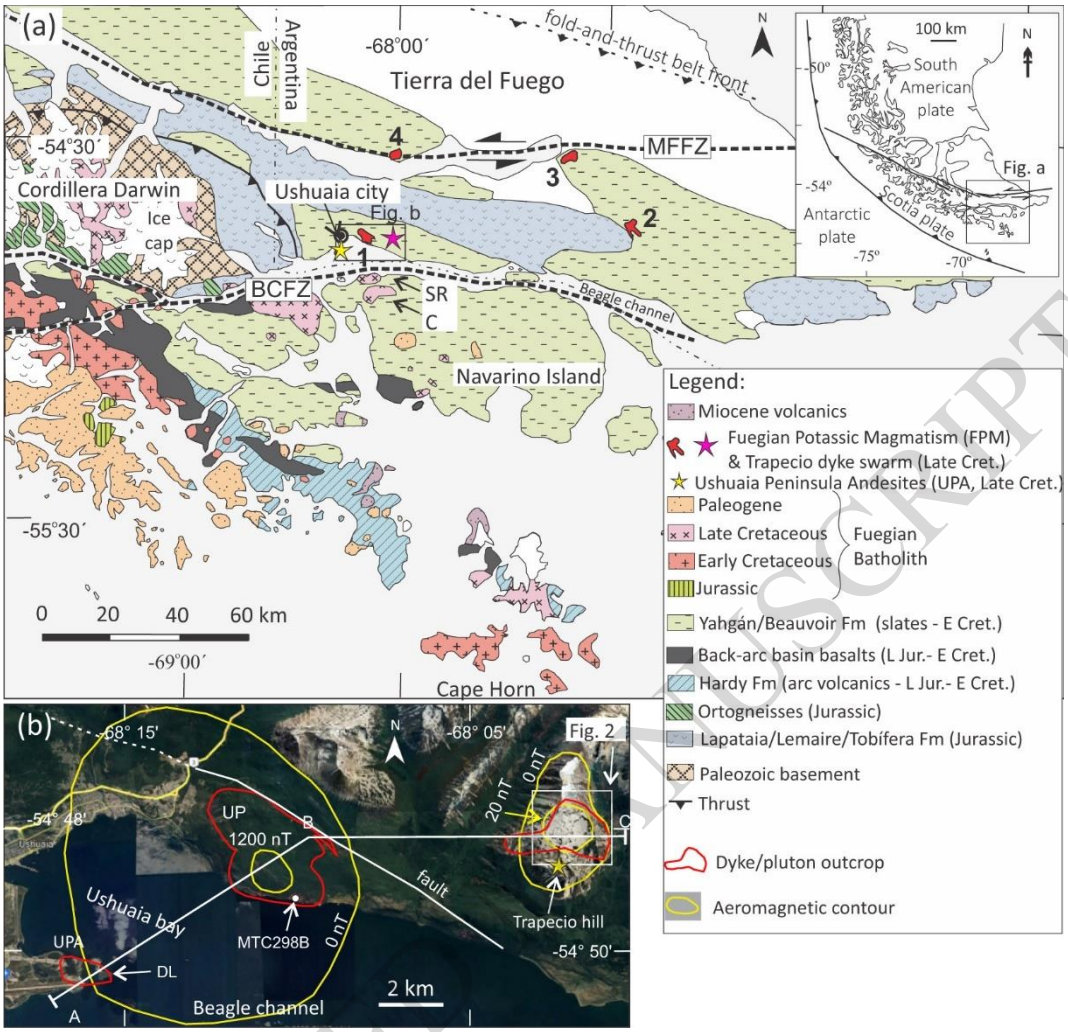

Figure 2

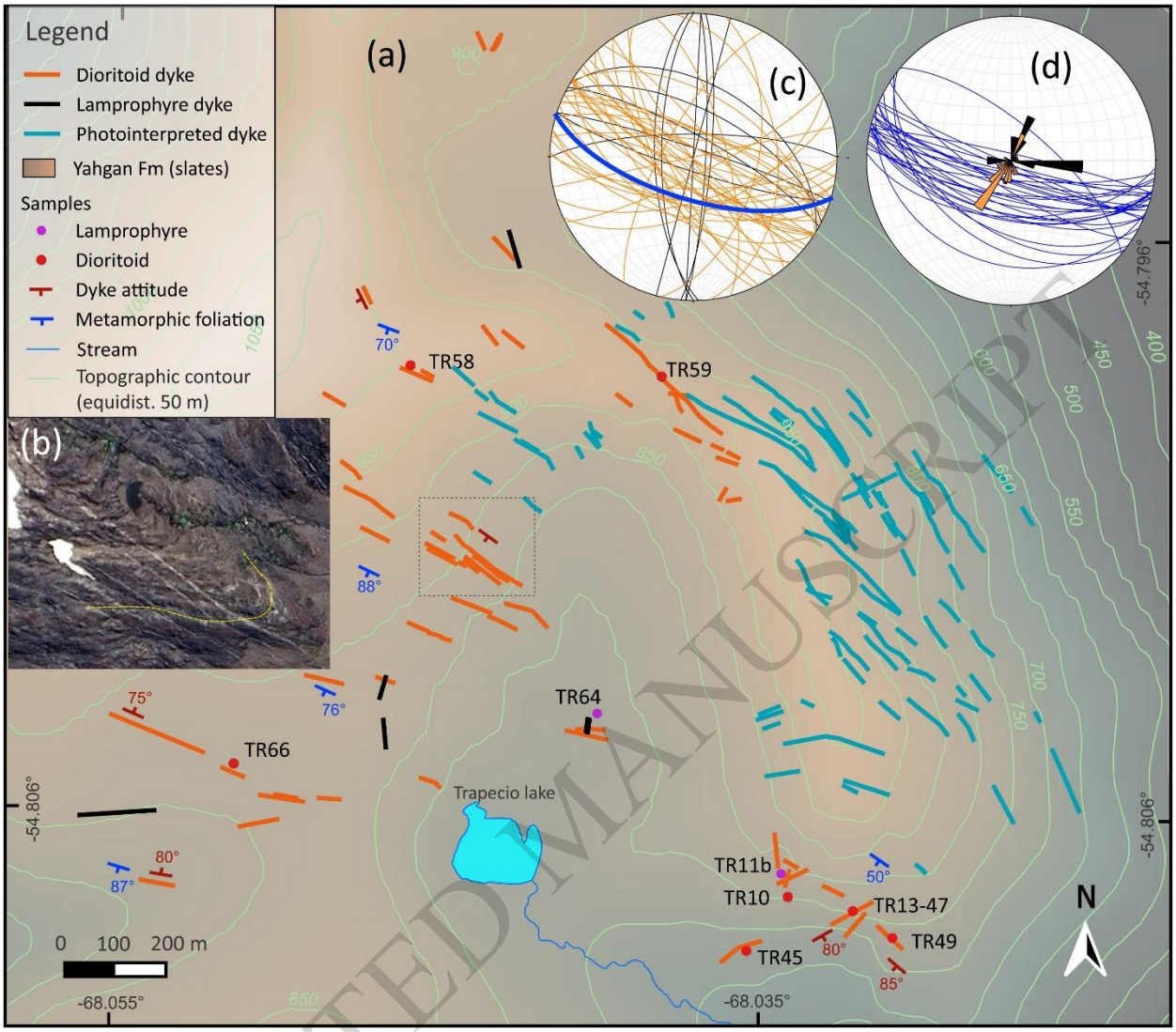

Figure 3

Figure 4

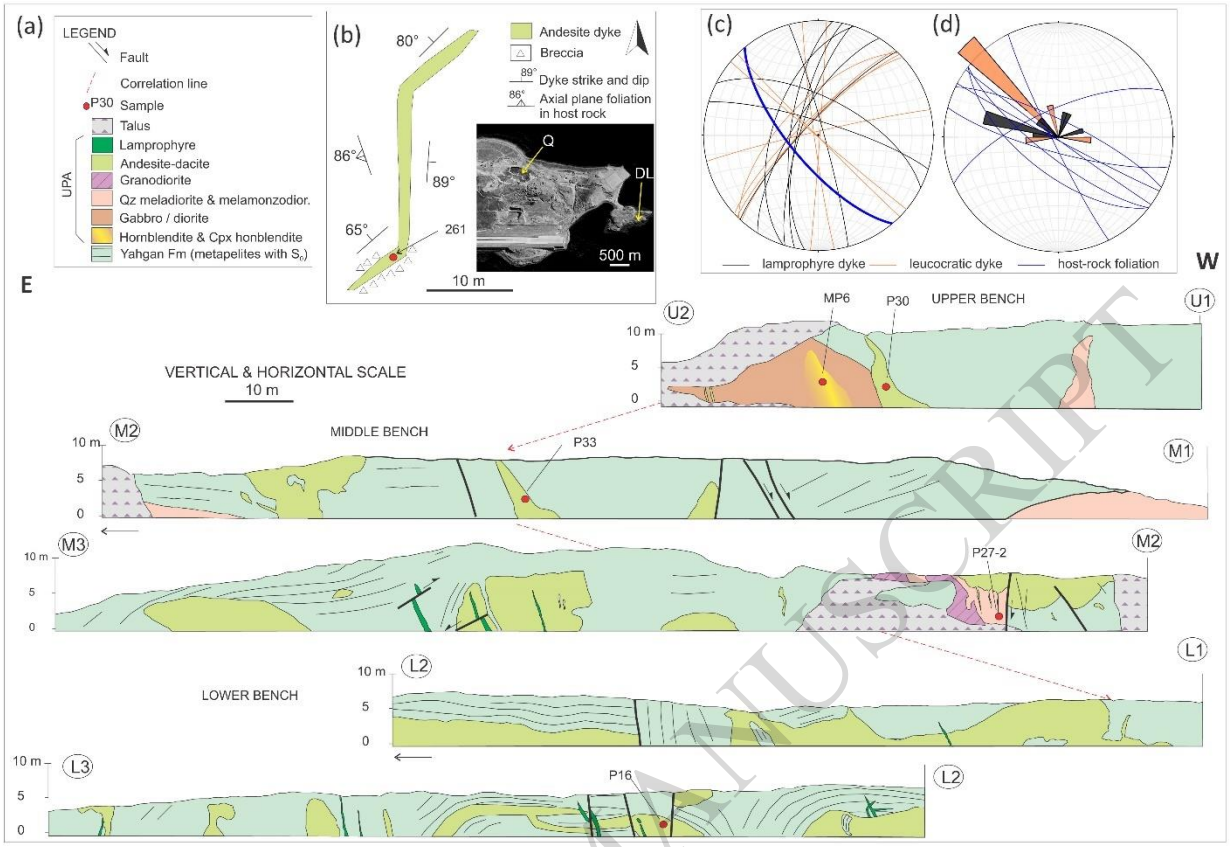

Figure 5

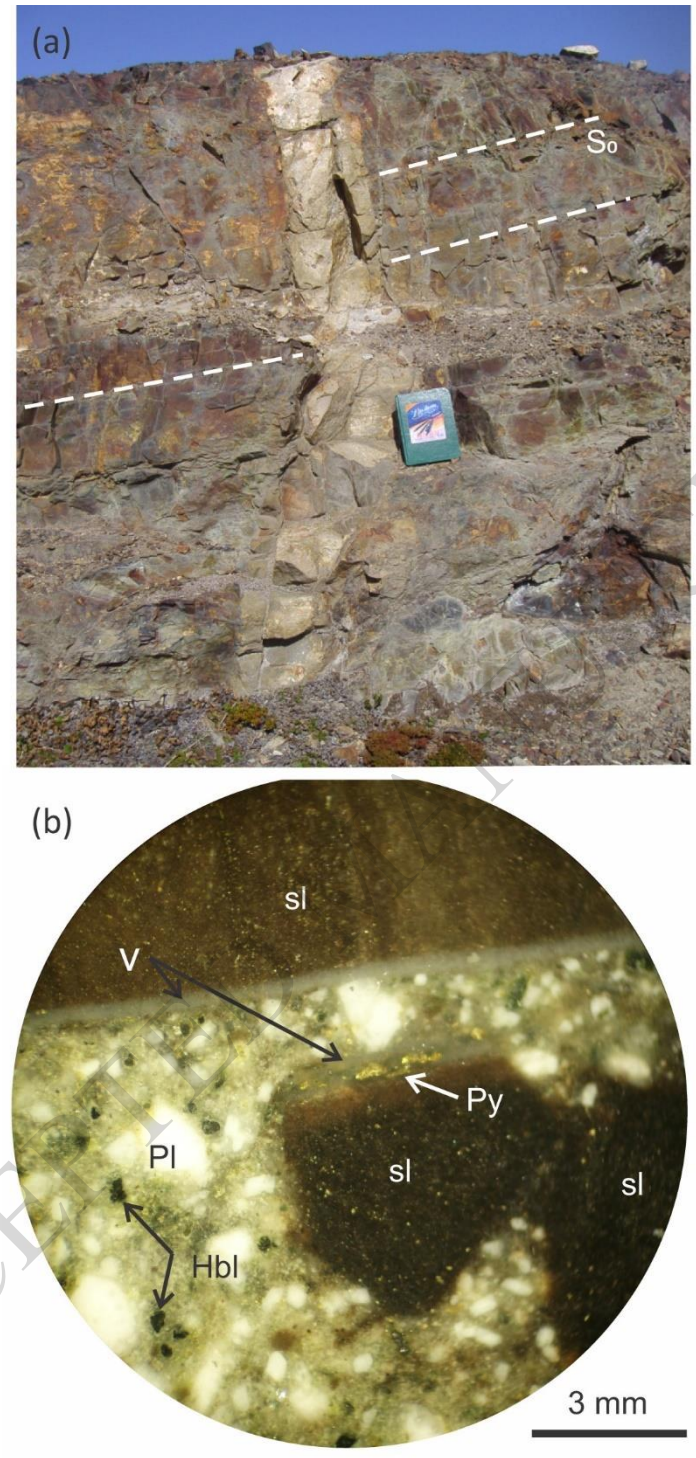

Figure 6

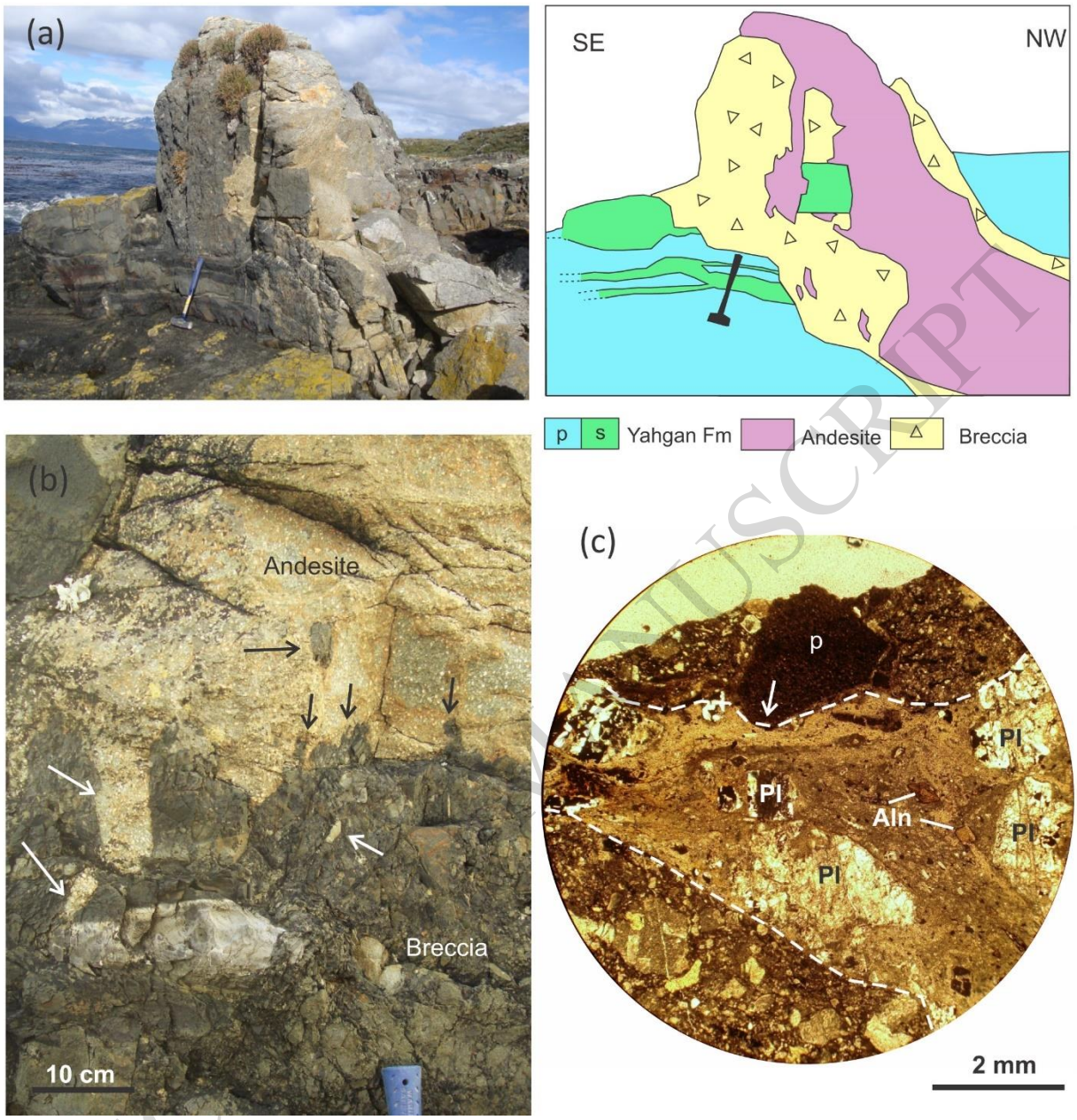

Figure 7

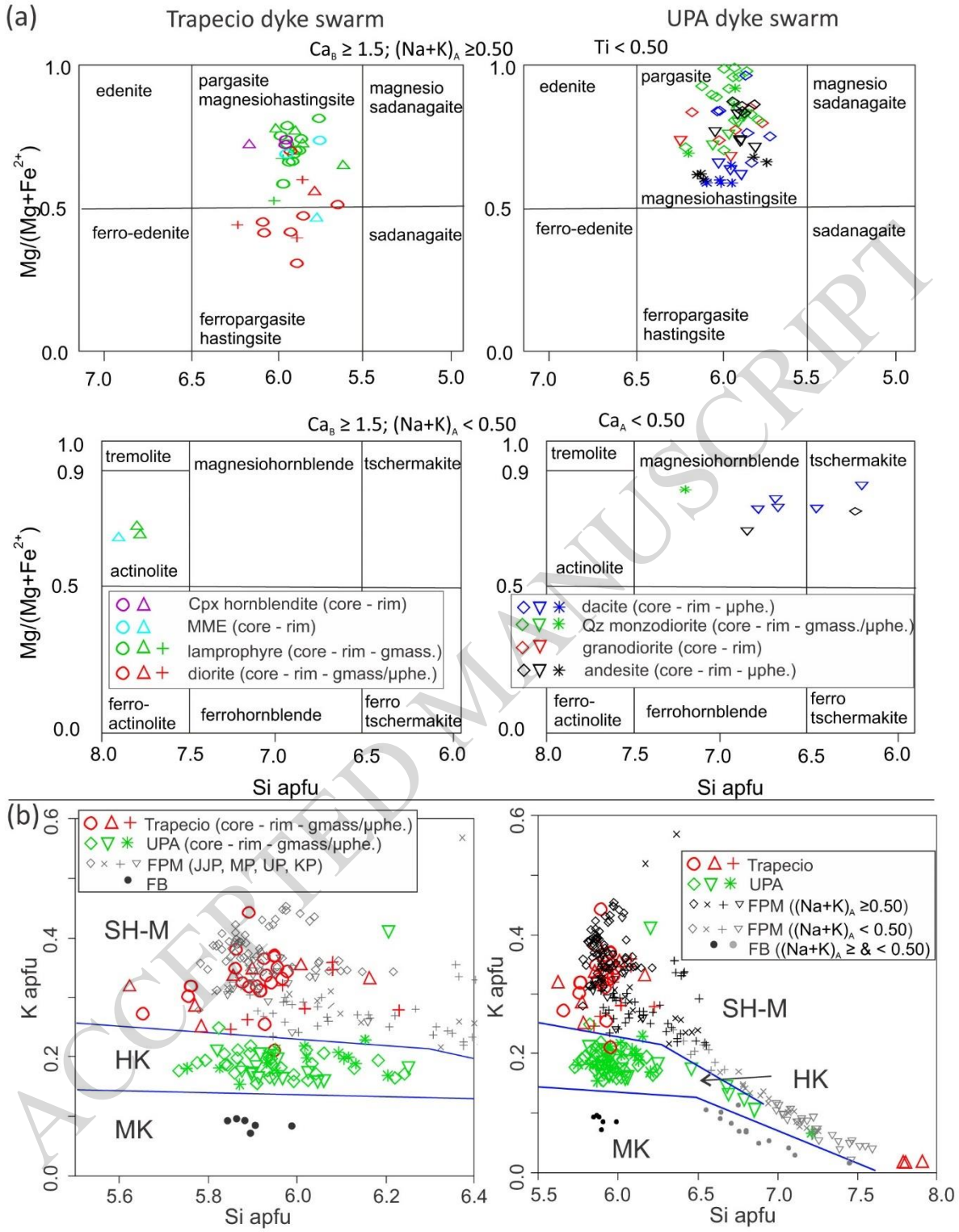

Figure 8

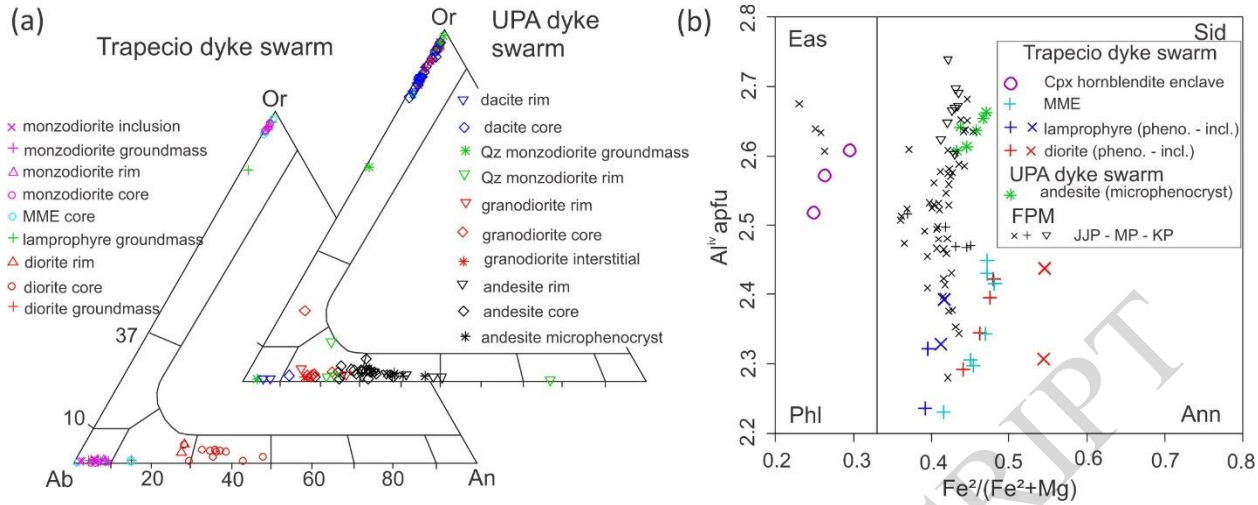

Figure 9

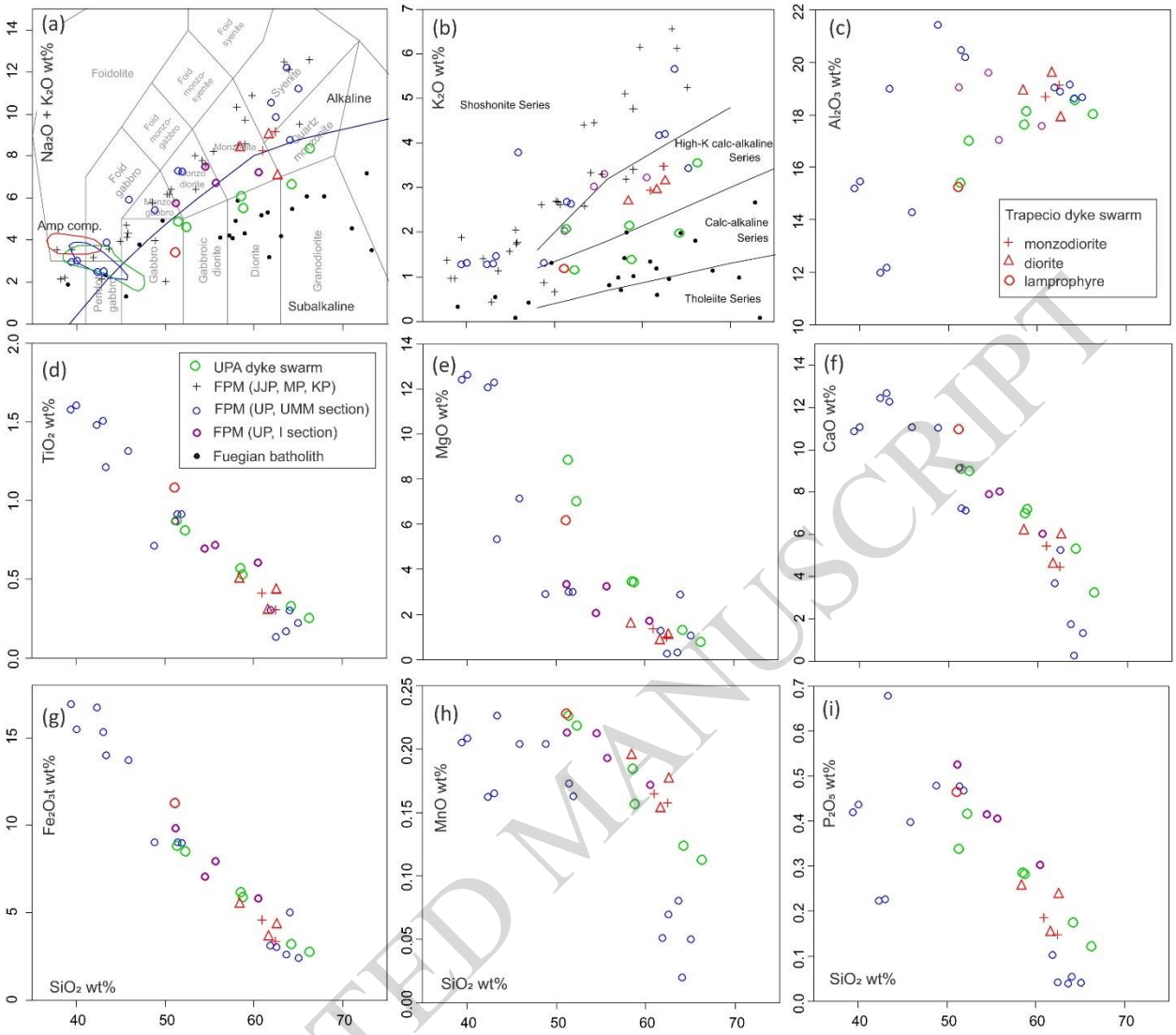

Figure 10

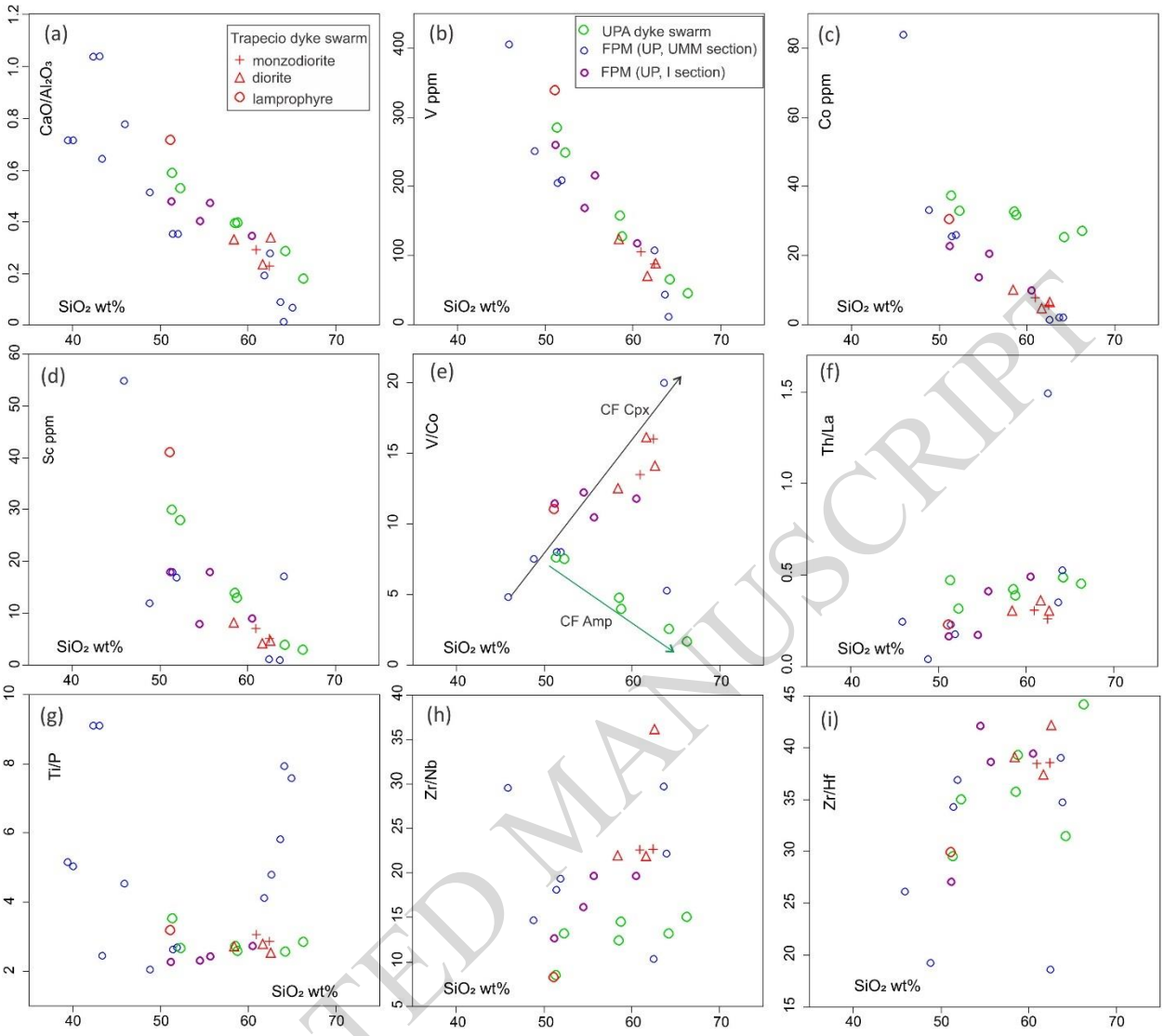

Figure 11

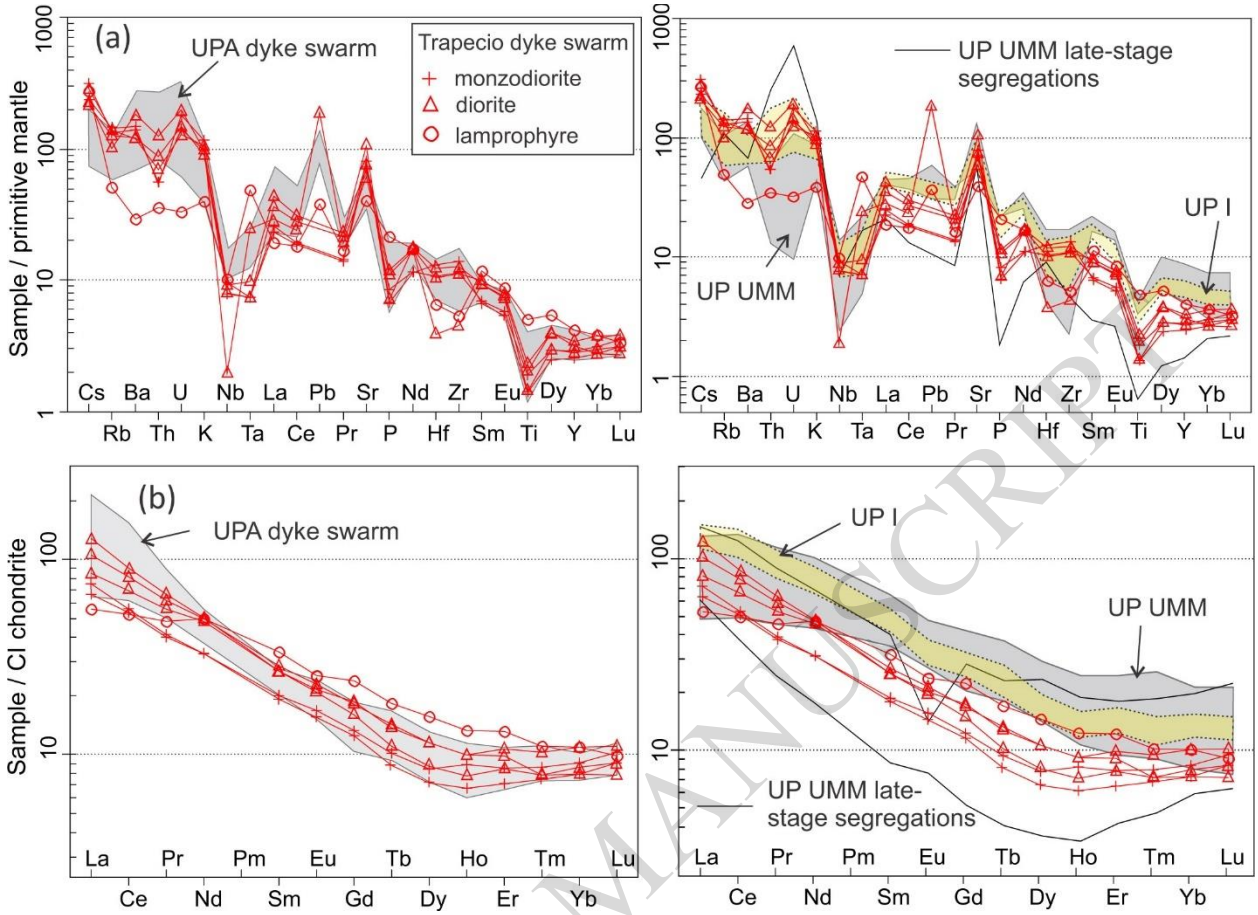

Figure 12

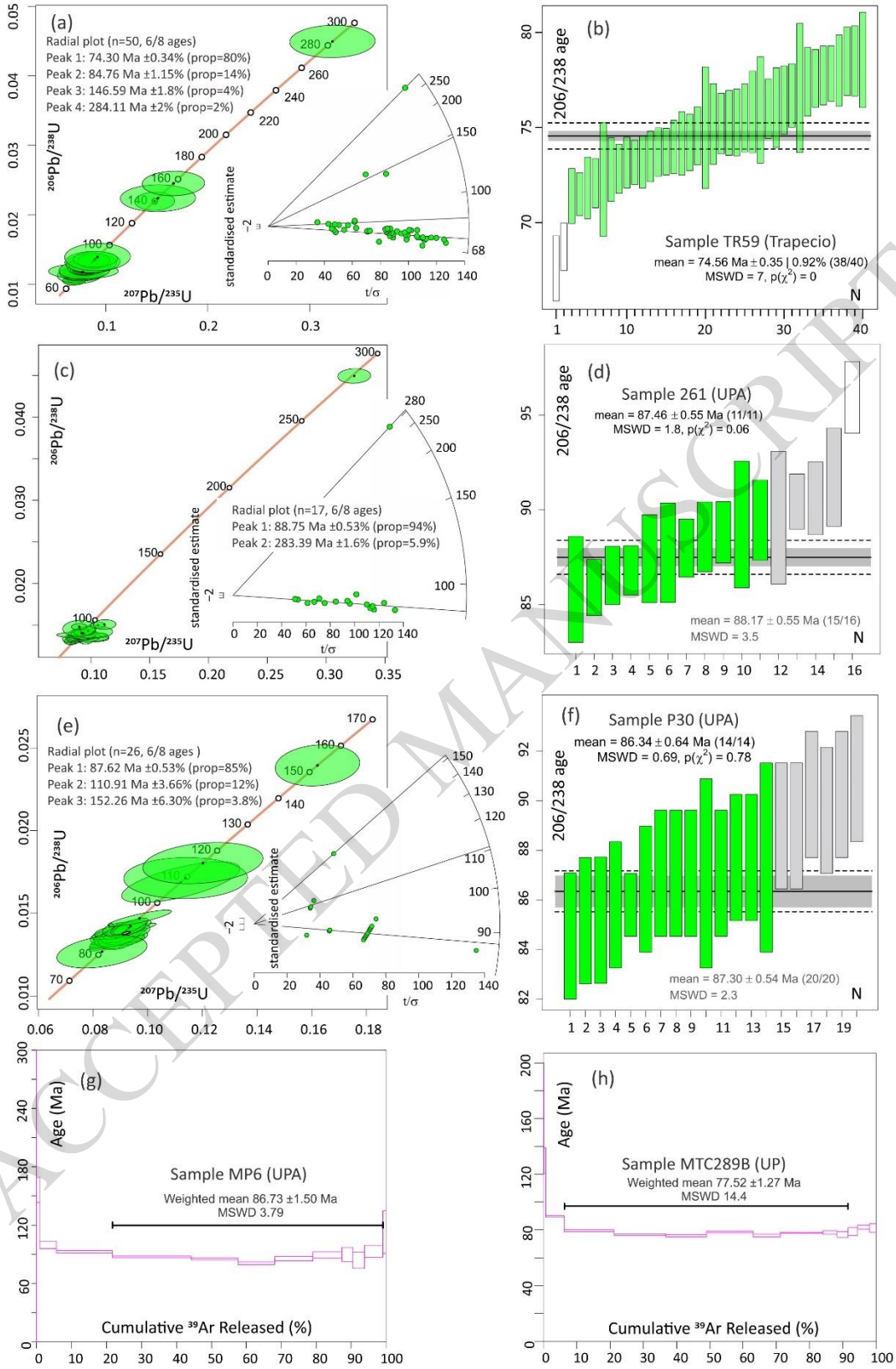

Figure 13